



An ALMA Survey of the SCUBA-2 Cosmology Legacy Survey UKIDSS/UDS Field: The Far-infrared/Radio Correlation for High-redshift Dusty Star-forming Galaxies

H. S. B. Algera¹, I. Smail², U. Dudzevičiūtė², A. M. Swinbank², S. Stach², J. A. Hodge¹, A. P. Thomson³, O. Almaini⁴, V. Arumugam⁵, A. W. Blain⁶, G. Calistro-Rivera⁷, S. C. Chapman⁸, C.-C. Chen⁹, E. da Cunha^{10,11,12},

D. Farrah^{13,14}, S. Leslie¹, D. Scott¹⁵, D. van der Vlugt¹, J. L. Wardlow¹⁶, and P. van der Werf¹

¹Leiden Observatory, Leiden University, P.O. Box 9513, 2300 RA Leiden, The Netherlands; algera@strw.leidenuniv.nl

²Centre for Extragalactic Astronomy, Durham University, Department of Physics, South Road, Durham DH1 3LE, UK

³The University of Manchester, Oxford Road, Manchester, M13 9PL, UK

⁴School of Physics and Astronomy, University of Nottingham, University Park, Nottingham NG7 2RD, UK

⁵Institut de Radioastronomie Millimétrique, 300 rue de la Piscine, Domaine Universitaire, F-38406 Saint Martin d'Hères, France

⁶Department of Physics and Astronomy, University of Leicester, University Road, Leicester LE1 7RH, UK

⁷European Southern Observatory, Karl-Schwarzschild-Strasse 2, D-85748, Garching bei München, Germany

⁸Department of Physics and Atmospheric Science, Dalhousie, Halifax, NS B3H 4R2, Canada

⁹Academia Sinica Institute of Astronomy and Astrophysics, No. 1, Sec. 4, Roosevelt Rd., Taipei 10617, Taiwan

¹⁰International Centre for Radio Astronomy Research, University of Western Australia, 35 Stirling Hwy, Crawley, WA 6009, Australia

¹¹Research School of Astronomy and Astrophysics, The Australian National University, Canberra, ACT 2611, Australia

¹²ARC Centre of Excellence for All Sky Astrophysics in 3 Dimensions (ASTRO 3D), Australia

¹³Department of Physics and Astronomy, University of Hawaii, 2505 Correa Road, Honolulu, HI 96822, USA

¹⁴Institute for Astronomy, 2680 Woodlawn Drive, University of Hawaii, Honolulu, HI 96822, USA

¹⁵Department of Physics and Astronomy, University of British Columbia, 6224 Agricultural Road, Vancouver, BC V6T 1Z1, Canada

¹⁶Physics Department, Lancaster University, Lancaster LA14YB, UK

Received 2020 June 23; revised 2020 September 9; accepted 2020 September 9; published 2020 November 11

Abstract

We study the radio properties of 706 submillimeter galaxies (SMGs) selected at $870\ \mu\text{m}$ with the Atacama Large Millimeter Array from the SCUBA-2 Cosmology Legacy Survey map of the Ultra Deep Survey field. We detect 273 SMGs at $>4\sigma$ in deep Karl G. Jansky Very Large Array 1.4 GHz observations, of which a subset of 45 SMGs are additionally detected in 610 MHz Giant Metre-Wave Radio Telescope imaging. We quantify the far-infrared/radio correlation (FIRRC) through parameter q_{IR} , defined as the logarithmic ratio of the far-infrared and radio luminosity, and include the radio-undetected SMGs through a stacking analysis. We determine a median $q_{\text{IR}} = 2.20 \pm 0.03$ for the full sample, independent of redshift, which places these $z \sim 2.5$ dusty star-forming galaxies 0.44 ± 0.04 dex below the local correlation for both normal star-forming galaxies and local ultraluminous infrared galaxies (ULIRGs). Both the lack of redshift evolution and the offset from the local correlation are likely the result of the different physical conditions in high-redshift starburst galaxies, compared to local star-forming sources. We explain the offset through a combination of strong magnetic fields ($B \gtrsim 0.2$ mG), high interstellar medium (ISM) densities and additional radio emission generated by secondary cosmic rays. While local ULIRGs are likely to have similar magnetic field strengths, we find that their compactness, in combination with a higher ISM density compared to SMGs, naturally explains why local and high-redshift dusty star-forming galaxies follow a different FIRRC. Overall, our findings paint SMGs as a homogeneous population of galaxies, as illustrated by their tight and nonevolving far-infrared/radio correlation.

Unified Astronomy Thesaurus concepts: [High-redshift galaxies \(734\)](#); [Starburst galaxies \(1570\)](#); [Galaxy evolution \(594\)](#)

1. Introduction

The most vigorously star-forming galaxies in the universe are known to be highly dust-enshrouded, and as such reprocess the bulk of the ultra-violet (UV) radiation associated with massive star formation to emission at rest-frame far-infrared (FIR) wavelengths. While in the local universe these galaxies contribute little to cosmic star formation (e.g., Blain et al. 2002), early submillimeter surveys discovered they were orders of magnitude more numerous at high redshift (Smail et al. 1997; Hughes et al. 1998; Barger et al. 1998). Accordingly, these distant, dust-enshrouded galaxies were dubbed submillimeter galaxies (SMGs; Blain et al. 2002). The submillimeter surveys leading to their discovery were limited in angular resolution, complicating the identification of counterparts to SMGs at other wavelengths. An effective way around this difficulty was provided by follow-up radio observations with high enough resolution allowing for a less ambiguous determination of the

origin of the FIR emission (Ivison et al. 1998; Smail et al. 2000; Lindner et al. 2011; Barger et al. 2012). This approach relies on the close connection between the total IR output and radio luminosity of star-forming galaxies that has been known to exist for decades (van der Kruit 1971, 1973; de Jong et al. 1985; Helou et al. 1985; Condon 1992; Yun et al. 2001; Bell 2003). The existence of this FIR/radio correlation (FIRRC) is a natural outcome if galaxies are “calorimeters,” as proposed initially by Völk (1989) and Lisenfeld et al. (1996). In this model, galaxies are fully internally opaque to the UV radiation arising from massive star formation, such that these UV photons are reprocessed by dust in the galaxy’s interstellar medium (ISM), and subsequently re-radiated in the FIR. For this reason, FIR emission is a robust tracer of recent ($\lesssim 100$ Myr; e.g., Kennicutt 1998) star formation, provided the galaxy is optically thick to UV photons. Since these very same massive stars ($M_* \sim 8\text{--}40 M_\odot$; Heger et al. 2003) end their lives in Type-II supernovae, the resulting energetic cosmic rays traverse

through the galaxy’s magnetic field and lose energy via synchrotron emission. Provided only a small fraction of cosmic rays escape the galaxy before cooling, a correlation between the FIR and radio emission of a star-forming galaxy naturally arises (Völk 1989).

The ubiquity and apparent tightness of this correlation across a wide range of galaxy luminosities allows for the use of radio emission as an indirect indicator of dust-obscured star formation, and as such it has been widely utilized to study the history of cosmic star formation (e.g., Haarsma et al. 2000; Smolčić et al. 2009; Karim et al. 2011; Novak et al. 2017). This application of the FIRRC at high redshift, however, requires a clear understanding of whether it evolves across cosmic time. From a theoretical point of view, such evolution is indeed expected. For example, the increased energy density of the cosmic microwave background (CMB) at high redshift is expected to suppress radio emission in star-forming galaxies, as cosmic rays will experience additional cooling from inverse Compton scattering off the CMB (e.g., Murphy 2009; Lacki & Thompson 2010). The exact magnitude of this process, however, will depend on the magnetic field strengths of the individual galaxies, which—especially at high redshift—are poorly understood. From an observational perspective, significant effort has been undertaken to assess whether the FIRRC evolves throughout cosmic time. While a number of studies find no evidence for such evolution (e.g., Ivison et al. 2010b; Sargent et al. 2010; Mao et al. 2011; Duncan et al. 2020), some studies suggest redshift evolution in the FIRRC in the opposite sense to what is expected theoretically (Ivison et al. 2010a; Thomson et al. 2014; Magnelli et al. 2015; Delhaize et al. 2017; Calistro Rivera et al. 2017; Ocran et al. 2020), seemingly implying that high-redshift ($z \gtrsim 1$) star-forming galaxies have increased radio emission (or, alternatively, decreased FIR emission) compared to their local counterparts.

The most obvious explanation of this apparent evolution is contamination of the observed radio luminosity by emission from an active galactic nucleus (AGN) in the galaxy (e.g., Murphy et al. 2009). While such emission is straightforward to identify for radio-loud AGNs—precisely because it drives a galaxy away from the FIRRC—composite sources may exhibit only low-level AGN activity, making them difficult to distinguish from typical star-forming galaxies (e.g., Beswick et al. 2008; Padovani et al. 2009; Bonzini et al. 2013). A major uncertainty of the applicability of the FIRRC is therefore one’s ability to identify radio AGNs, which is generally more challenging at high redshift. An additional potential driver of apparent redshift evolution of the FIRRC involves sample selection (e.g., Sargent et al. 2010). Differences in the relative depths of the radio and FIR observations, if not properly taken into account, will result in a biased sample. Additionally, the sensitivity of radio and FIR surveys to galaxies at high redshift are typically substantially different. While (sub-)mm surveys are nearly uniformly sensitive to dust-obscured star formation across a wide range of redshifts ($1 \lesssim z \lesssim 10$; Blain et al. 2002) and predominantly select galaxies at $z \approx 2-3$ (e.g., Chapman et al. 2005; Dudzevičiūtė et al. 2020) owing to the strong, negative K -correction, radio surveys instead suffer from a positive K -correction (Condon 1992), and therefore predominantly select sources around $z \sim 1$ (Condon 1989). Evidently, such selection biases must be addressed in order to assess the evolution of the FIRRC in the early universe.

The cleanest way of studying any evolution in the FIRRC is therefore to start from a sample where the selection is well

understood, and where radio AGNs are less of a complicating factor. For this purpose, we employ the ALMA¹⁷ SCUBA-2 Ultra Deep Survey (UDS) (AS2UDS), which constitutes the largest, homogeneously selected, sample of SMGs currently available (Stach et al. 2019; Dudzevičiūtė et al. 2020). While the FIRRC has been studied using FIR-selected samples before (e.g., Ivison et al. 2010a, 2010b; Thomson et al. 2014), the extent to which it evolves with cosmic time has remained unclear, due to either the limited resolution of the FIR data, the modest available sample sizes, or biases in these samples. The more than 700 ALMA-detected SMGs from the AS2UDS survey improve upon these shortcomings, and hence allow for a detailed investigation of the FIRRC for strongly star-forming sources at high redshift.

The structure of this paper is as follows. In Section 2 we outline the submillimeter and radio observations of the AS2UDS sample. In Section 3, we separate radio AGNs from our sample, and investigate the redshift evolution of the star-forming SMGs. In Section 4 we discuss our results in terms of the physical properties of SMGs. Finally, we present our conclusions in Section 5. Throughout this paper, we adopt a flat Λ -CDM cosmology, with $\Omega_m = 0.30$, $\Omega_\Lambda = 0.70$ and $H_0 = 70 \text{ km s}^{-1} \text{ Mpc}^{-1}$. We further assume a Chabrier (2003) initial mass function, quote magnitudes in the AB system, and define the radio spectral index α such that $S_\nu \propto \nu^\alpha$, where S_ν represents the flux density at frequency ν .

2. Observations and Methods

2.1. Submillimeter Observations

The AS2UDS survey (Stach et al. 2019) constitutes a high-resolution follow-up with ALMA of SCUBA-2 850 μm sources originally detected over the UKIDSS UDS field as part of the SCUBA-2 Cosmology Legacy Survey (S2CLS; Geach et al. 2017). The parent single-dish submillimeter survey spans an area of 0.96 deg^2 , to a median depth of $\sigma_{850} = 0.88 \text{ mJy beam}^{-1}$. All sources detected at a significance of $>4\sigma$ ($S_{850} \geq 3.6 \text{ mJy}$) were targeted with ALMA observations in Band 7 (344 GHz or 870 μm) across four different cycles (1, 3, 4, 5). As a result, the beam size of the data varies between $0''.15$ and $0''.5$, though for source detection all images were homogenized to $0''.5$ FWHM. Further details of the survey strategy and data reduction are presented in Stach et al. (2019). The final submillimeter catalog contains 708 SMGs detected at $\geq 4.3\sigma$ ($S_{870} > 0.9 \text{ mJy}$), with an estimated false-positive rate of 2%.

2.2. Radio Observations

The UDS field has been observed at 1.4 GHz by the Karl G. Jansky Very Large Array (VLA). These observations will be fully described in V. Arumugam et al. (2020, in preparation) and are additionally briefly summarized in Thomson et al. (2019) and Dudzevičiūtė et al. (2020). In short, the 1.4 GHz image consists of a 14-pointing mosaic, for a total integration time of ~ 160 hr, across multiple VLA configurations. The bulk of the data (~ 110 hr) were taken in A-configuration, augmented by ~ 50 hr of observations in VLA B-array and ~ 1.5 hr in the DnC configuration. The final root-mean-square (rms) noise in the map is nearly uniform, reaching $7 \mu\text{Jy beam}^{-1}$ in the image center, up to $10 \mu\text{Jy beam}^{-1}$ near the mosaic edges. The resulting synthesized beam is well described by an elliptical

¹⁷ Atacama Large Millimeter/submillimeter Array.

Gaussian with major and minor axes of, respectively, $1''.8$ and $1''.6$. The final flux densities have been corrected for bandwidth-smearing, to be described in detail in V. Arumugam et al. (2020, in preparation), and are provided for the AS2UDS sources by Dudzevičiūtė et al. (2020). Overall, 706/708 SMGs fall within the 1.4 GHz radio footprint covering the UDS field. These sources form the focus of this work.

The UDS field has further been targeted at 610 MHz by the Giant Metre-Wave Telescope (GMRT) during 2006 February 3–6 and December 5–10. Details of the data reduction and imaging are provided in Ibar et al. (2009). In summary, the GMRT image comprises a three-pointing mosaic, with each pointing accounting for 12 hr of observing time. The final rms noise of the 610 MHz mosaic is $45 \mu\text{Jy beam}^{-1}$ in the image center, and reaches up to $80 \mu\text{Jy beam}^{-1}$ near the edges, for a typical value of $65 \mu\text{Jy beam}^{-1}$. The synthesized beam of the image is well described by a slightly elliptical Gaussian of size $6''.1 \times 5''.1$. A total of 689 SMGs fall within the footprint of the 610 MHz observations. Source detection is performed using PYBDSF (Mohan & Rafferty 2015), down to a peak threshold of 4.0σ , leading to the identification of a total of 853 radio sources, though only a small fraction of those are associated with AS2UDS SMGs (Section 3). Due to the large beam size, the counterparts of AS2UDS SMGs are unresolved at 610 MHz, and as such we adopt peak flux densities for all of them. We further verify that source blending is not an issue, as only 2% of AS2UDS SMGs have more than one radio-detected source at 1.4 GHz in their vicinity within a GMRT beam full-width half maximum. In addition, for a source to be detected at 610 MHz, but not at 1.4 GHz, requires an unphysically steep spectral index of $\alpha \approx -2.7$, very different from the typical radio spectral index of $\alpha \sim -0.80$ (Condon 1992; Ibar et al. 2010; see also Section 3). As a result, the VLA map is sufficiently deep that further confusion or flux boosting at 610 MHz can also be ruled out when no radio counterpart is detected at 1.4 GHz.

2.3. Additional Multiwavelength Data

In order to investigate the physical properties of our SMG sample, it is crucial to obtain panchromatic coverage of their spectral energy distributions (SEDs). At UV, optical and near-IR wavelengths, these SEDs are dominated by (dust-attenuated) stellar emission, which includes spectral features that are critical for obtaining accurate photometric redshifts. As SMGs are typically high redshift in nature ($z \approx 2-3$; e.g., Chapman et al. 2005; Danielson et al. 2017), these rest-frame wavelengths can be probed with near- and mid-IR observations. The multiwavelength coverage of the UDS field, as well as the association of counterparts to the SMG sample, is described in detail in Dudzevičiūtė et al. (2020), and further summarized in their Table 1, although we briefly repeat the key points here.

Dudzevičiūtė et al. (2020) collated optical/near-IR photometry for the AS2UDS SMGs from the 11th UDS data release (UKIDSS DR11; O. Almaini et al. 2020, in preparation). DR11 constitutes a K -band-selected photometric catalog covering an area of 0.8 deg^2 . The K -band image reaches a 3σ depth of 25.7 mag, in $2''$ diameter apertures, and the resulting photometric catalog contains nearly 300,000 sources. This catalog further contains photometry in the J - and H -bands from the UKIRT WFCAM, as well as Y -band observations from VISTA/VIDEO, $BVRi'z'$ -band photometry from Subaru/Suprimecam, and U -band

observations from the Canada–France–Hawaii Telescope/Megacam survey.

In total, 634 SMGs lie within the area covered by deep K -band imaging. The ALMA and K -band-selected catalogs have been cross-matched using a radius of $0''.6$, resulting in 526/634 associations with an expected false-match rate of 3.5%. A significant number of SMGs, 17%, are hence undetected even in deep K -band imaging (see Smail et al. 2020). Further imaging in the infrared is provided by Spitzer, in the four IRAC channels, as well as MIPS $24 \mu\text{m}$, as part of the Spitzer Legacy Program (SPUDS, PI: J. Dunlop). Upon adopting a conservative blending criterion where SMGs with nearby K -band detections are treated as upper limits (see Dudzevičiūtė et al. 2020 for details), 73% of the SMGs covered by the IRAC maps are detected at $3.6 \mu\text{m}$. In total, 48% of SMGs are further detected at $24 \mu\text{m}$.

While the AS2UDS sample is, by construction, detected in the submillimeter at $870 \mu\text{m}$, additional sampling of the long-wavelength dust continuum is crucial in order to obtain accurate FIR luminosities, as well constraints on SMG dust properties, such as dust masses and temperatures. For this purpose, we employ observations taken with the PACS and SPIRE instruments aboard the Herschel Space Observatory. To compensate for the coarse point-spread function at these wavelengths and the resulting source blending, Dudzevičiūtė et al. (2020) deblended the data following Swinbank et al. (2014), adopting ALMA, Spitzer/MIPS $24 \mu\text{m}$, and 1.4 GHz observations as positional priors. Overall, 68% of ALMA SMGs have a measured (potentially deblended) flux density in at least one of the PACS or SPIRE bands.

2.4. SMG Redshifts and Physical Properties

The redshift distributions, as well as numerous other physical properties of the AS2UDS SMGs, have been investigated by Dudzevičiūtė et al. (2020). For this, they employ the SED-fitting code MAGPHYS (da Cunha et al. 2008, 2015; Battisti et al. 2019), which is designed to fit the full UV-to-radio SED of star-forming galaxies. In order to self-consistently constrain the SED, MAGPHYS employs an energy balance procedure, whereby emission in the UV, optical, and near-IR is physically coupled to the emission at longer wavelengths by accounting for absorption and scattering by dust within the galaxy. The star formation histories of individual galaxies are modeled as a delayed exponential function, following Lee et al. (2010), which corresponds to an initial linearly increasing star formation rate, followed by an exponential decline. In addition, it allows for bursts to be superimposed on top this continuous star formation history, during which stars are formed at a constant rate for up to 300 Myr. We note, however, that constraining the star formation history and assigning ages by fitting to the broadband photometry of strongly dust-obscured galaxies is notoriously challenging (e.g., Hainline et al. 2011; Michałowski et al. 2012; Simpson et al. 2014). Further details of the MAGPHYS analysis, including an extensive description of calibration and testing, are provided in Dudzevičiūtė et al. (2020).

The latest extension of MAGPHYS, presented in Battisti et al. (2019), further incorporates fitting for the photometric redshifts of galaxies. Accurate redshift information is crucial for a complete characterization of the SMG population, as any uncertainties on a galaxy's redshift will propagate into the error on derived physical quantities. Incorporating FIR data in the fitting can further alleviate degeneracies between optical colors and redshift, potentially allowing for a more robust determination of photometric redshifts (Battisti et al. 2019). This is

especially relevant for SMGs, as these typically constitute an optically faint population.

In total, 44 AS2UDS SMGs have a measured spectroscopic redshift. Dudzevičiūtė et al. (2020) compared the photometric redshifts (derived for both this SMG sub-sample, as well as for around 7000 field galaxies in the UDS field with spectroscopic redshifts) to the existing spectroscopic ones, and found a photometric accuracy of $\Delta z / (1 + z_{\text{spec}}) = -0.005 \pm 0.003$. Hence, the photometric redshifts provided by MAGPHYS are in excellent agreement with the spectroscopic values. The typical uncertainty on the photometric redshift for the AS2UDS SMGs is $\Delta z \approx 0.25$.

Finally, various physical quantities are determined for the SMG sample via MAGPHYS, including star formation rates, mass-weighted ages, stellar and dust masses, as well as FIR luminosities. The accuracy of these values has been assessed by Dudzevičiūtė et al. (2020) through comparing with simulated galaxies from EAGLE (Crain et al. 2015; Schaye et al. 2015; McAlpine et al. 2019), where these properties are known a priori. The simulated and MAGPHYS-derived values for the various physical parameters are typically in good agreement.

We caution that MAGPHYS does not allow for any contribution from an AGN to the overall SED. In particular, emission from a mid-IR power-law component, indicative of an AGN torus, may therefore result in slightly boosted FIR emission. Such a mid-IR power law is, however, not expected to contaminate the observed $870 \mu\text{m}$ (rest-frame $\sim 250 \mu\text{m}$) flux density (e.g., Lyu & Rieke 2017; Xu et al. 2020), and as such does not affect our sample selection. Therefore, we can quantify the typical contribution of the mid-IR power law to the total IR luminosity for the AS2UDS SMGs. For this, we limit ourselves to the 442 SMGs at $z \leq 3.0$, following Stach et al. (2019), since above this redshift the criteria are prone to misclassifying dusty star-forming galaxies. This constitutes a total of 82 sources (12% of the full AS2UDS sample). We find the median 8–1000 μm luminosity to be $\log_{10} L_{\text{FIR}} = 12.54^{+0.07}_{-0.04} L_{\odot}$ and $\log_{10} L_{\text{FIR}} = 12.33^{+0.02}_{-0.03} L_{\odot}$ for sources with and without a mid-IR power law, respectively. We therefore conclude that the typical AGN contribution to the total IR luminosity is at most $\lesssim 0.2$ dex.

An additional diagnostic of an AGN is luminous X-ray emission. However, only one-third of the AS2UDS SMGs lie within the footprint of the available Chandra X-ray imaging as part of the X-UDS survey (Kocevski et al. 2018; see also Stach et al. 2019). In particular, out of the 23 SMGs associated with strong X-ray emitters, 18 are additionally identified as AGNs through their mid-IR power-law emission. Therefore, when discussing AGNs in the SMG population, we focus on the 82 mid-IR-selected sources, which make up the bulk of the AGNs in the AS2UDS sample.

Studies of radio-selected samples have shown that AGN activity at radio wavelengths is often disjoint from AGN-related emission at X-ray and mid-IR wavelengths (e.g., Delvecchio et al. 2017; Algera et al. 2020). In particular, Algera et al. (2020) show that radio sources with X-ray and/or mid-IR power-law emission fall onto the same FIRRC as “clean” star-forming sources. For this reason, we have decided to retain sources with nonradio AGN signatures in our sample (Section 3.2). In all relevant figures in this work, we however distinguish between “clean SMGs” and sources with a mid-IR power-law signature via different plotting symbols. We additionally emphasize that our results are unaffected if these AGNs are removed from the analysis entirely.

2.5. Radio Stacking

A comprehensive analysis of the FIRRC requires addressing any biases in the sample selection. In particular, the majority of AS2UDS sources are not detected in the 1.4 GHz VLA map (about 60%; Section 3.1), yet their—a priori unknown—radio properties must still be included in the analysis. In this work, we employ a stacking technique in order to obtain a census of the typical radio properties of the AS2UDS sample.

For the stacking, we create cutouts of 51×51 pixels ($18'' \times 18''$) from the 1.4 GHz radio map, centered on the precise ALMA positions of the AS2UDS sources. We average these cutouts together by taking the median value across each pixel. In order to properly account for the full SMG population, we stack both the radio-detected and -undetected SMGs together. Additionally, we stack empty regions within the image, away from radio sources, to create an “empty” stack indicative of the background and typical rms value (following e.g., Decarli et al. 2014). We have verified that the rms is reduced following a typical $1/\sqrt{N}$ behavior, where N is the number of sources being stacked. This indicates we are not significantly affected by confusion noise. We pass both the real and empty stacks to PYBDSF (Mohan & Rafferty 2015) to obtain peak, integrated, and aperture flux densities. We have run extensive simulations, using mock sources inserted into the image plane, to ascertain which flux density is the correct one to use. We elaborate on these simulations in Appendix A, and will describe them in further detail in a future work (Algera et al. 2020). The simulations show that integrated fluxes provide the most robust flux measurement for our data at moderate signal-to-noise ratio ($S/N \gtrsim 10$). In this work, we therefore use integrated fluxes obtained from PYBDSF. The only exceptions are the GMRT 610 MHz stacks described in Section 3.3, since due to the large beam size (about $5''$) all stacks are unresolved, and peak and integrated flux densities are consistent. For the GMRT stacks, we therefore adopt peak flux densities.

In order to determine realistic uncertainties on the stacked flux densities, we perform a bootstrap analysis, whereby we repeat the procedure described above 100 times. This involves sampling SMGs from each bin with replacement, such that duplicate cutouts are allowed. In this way, the uncertainties on the final flux density reflect both the uncertainties on the photometry, as well as the intrinsic variation in the radio flux densities among the AS2UDS SMGs.

3. Results

3.1. Radio Properties of AS2UDS

In total, 273 out of the 706 SMGs in the 1.4 GHz coverage of AS2UDS (39%) can be cross-matched to a radio counterpart detected at $\geq 4\sigma$ at 1.4 GHz, within a matching radius of $1''.6$ (chosen such that the fraction of false positives is 1%; Dudzevičiūtė et al. 2020). This detection fraction is typical for high-redshift SMGs (e.g., Biggs et al. 2011; Hodge et al. 2013). We additionally detect 45 SMGs down to a 4σ threshold in the shallower 610 MHz observations. All of the sources detected in the 610 MHz map have a counterpart at 1.4 GHz, based on a cross-matching radius of $2''.0$. This is slightly larger than the matching radius adopted for the VLA radio data to account for the coarser GMRT 610 MHz resolution, but still ensures a small false positive fraction of $\lesssim 0.1\%$.

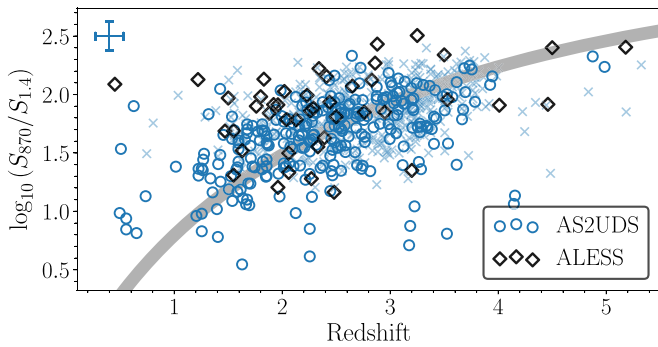


Figure 1. Ratio of the submillimeter to radio flux density as a function of redshift, for both the AS2UDS and ALESS samples. This ratio provides a crude proxy for redshift (Carilli & Yun 1999), as a result of the different typical K -corrections at 870 μm and 1.4 GHz. The expected trend with redshift is overlaid in gray, assuming a fixed far-infrared (FIR) luminosity, dust emissivity, and temperature, and FIR/radio correlation parameter q_{IR} (see text for details). In total, 273 (433 undetected) AS2UDS submillimeter galaxies are detected at $\geq 4\sigma$ (lower limits are shown as crosses) at 1.4 GHz, compared to 44 (32 undetected; not shown) for ALESS. The increase in sample size in comparison to ALESS constitutes nearly a factor of 10.

We present the FIR and radio properties of the AS2UDS sample in Figure 1, which shows the ratio of submillimeter to radio flux density for the AS2UDS SMGs as a function of redshift. As result of the different K -corrections in the FIR and radio, this ratio provides a crude proxy for redshift (e.g., Carilli & Yun 1999). The AS2UDS detections are consistent with the expected trend, plotted for a galaxy with a FIR luminosity of $10^{12.5} L_{\odot}$, which is typical for AS2UDS (Dudzevičiūtė et al. 2020). This further assumes a fixed dust emissivity and temperature of $\beta = 1.8$ and $T_{\text{dust}} = 35$ K, respectively, as well as a fixed radio spectral index of $\alpha = -0.8$ and a redshift-independent FIRRC, equal to the median value for AS2UDS (Section 3.3). There is, however, substantial scatter around this trend, as may be expected from intrinsic variations in the dust and radio properties of our SMG sample.

Figure 1 further emphasizes the substantial increase in sample size that AS2UDS provides compared to the ALESS survey (Hodge et al. 2013; Karim et al. 2013). The latter constitutes an ALMA follow-up of SMGs originally identified in the Extended Chandra Deep Field South as part of the LESS survey using the LABOCA bolometer (Weiß et al. 2009). ALESS is similar to AS2UDS in terms of sample selection, and therefore provides the best means of comparison for this work. Additionally, the depth of both its FIR and radio observations closely match that of AS2UDS. In total, the ALESS survey covers 76 SMGs within its radio footprint (Thomson et al. 2014). AS2UDS, therefore, constitutes a sample nearly 10 times larger than ALESS. We compare the combined FIR and radio properties of the AS2UDS and ALESS samples in Section 4.1.

We show the redshift distribution of the AS2UDS sources with radio detections in Figure 2 (left panel). As expected, the radio sources lie at a slightly lower redshift than the overall AS2UDS population, owing to the different K -corrections for typical radio- and submillimeter-detected sources. The median redshift of the 1.4 GHz-detected subsample is $\langle z \rangle = 2.44_{-0.15}^{+0.04}$, while that of the 45 GMRT-detected sources is $\langle z \rangle = 1.85_{-0.21}^{+0.24}$, compared to $\langle z \rangle = 2.62_{-0.04}^{+0.06}$ for the full sample of AS2UDS SMGs (Dudzevičiūtė et al. 2020).

We find a typical spectral index between 610 and 1400 MHz of $\alpha = -0.77_{-0.03}^{+0.05}$, consistent with the typical radio spectrum of star-forming galaxies of $\alpha \approx -0.80$ (e.g., Condon 1992; Ibar et al. 2010). Nevertheless, there is substantial variation in the spectra among the 45 sources detected at the two radio frequencies, with the 16th–84th percentile range spanning $\alpha \in [-1.19, -0.48]$. This range is wider than the variation expected based on the typical uncertainty on the spectral index of ~ 0.24 dex, indicating that at least some of this scatter is intrinsic variation in the radio spectral indices. The full distribution of spectral indices, including lower limits for sources detected solely at 1.4 GHz, is shown in the middle and right panels of Figure 2. These limits were calculated by adopting four times the local rms noise at the position of the radio source as an upper limit on the GMRT flux density. It is evident that most of the resulting lower limits on the spectral index are not very constraining, due to the limited depth of the 610 MHz data. In order to assign a spectral index to the entire radio-detected population, we median stack all AS2UDS SMGs detected solely at 1.4 GHz in both radio maps (225 sources within both the VLA and GMRT footprints). The typical stacked 610–1400 MHz spectral index is then found to be $\alpha = -0.81_{-0.23}^{+0.20}$. This value is consistent with the median spectral index obtained for the AS2UDS subsample having two radio detections, as well as with the typically assumed value of $\alpha = -0.80$ for SMGs. For ease of comparison to the literature, we will therefore adopt a fixed $\alpha = -0.80$ for all AS2UDS SMGs detected only in the 1.4 GHz map. We note that, while the beam size of our GMRT observations is significantly larger than that of the VLA data, the typical low-frequency radio sizes of SMGs are $\sim 0''.5$ – $1''.5$ (Miettinen et al. 2017; Jiménez-Andrade et al. 2019; Thomson et al. 2019), similar to the synthesized beam at 1.4 GHz. As such, this is much smaller than the largest angular scale to which we are sensitive with our data of $\sim 120''$ based on the ~ 50 hr of data taken in the VLA B-array configuration.¹⁸ Thomson et al. (2019) have further empirically verified the robustness of the theoretical largest angular scale and, as such, we do not expect to miss any diffuse emission at 1.4 GHz. Our spectral index measurements are therefore unaffected by the differing resolutions of our radio observations (see also Gim et al. 2019). We further discuss the spectral indices of the AS2UDS sample in Section 3.3.

Given these spectral indices for the radio-detected SMG subsample, we calculate the luminosity at a rest-frame frequency of $\nu = 1.4$ GHz as

$$L_{1.4} = \frac{4\pi D_L^2}{(1+z)^{1+\alpha}} S_{1.4}. \quad (1)$$

Here D_L is the luminosity distance to a source at redshift z , and $S_{1.4}$ is its flux density at the observer-frame frequency of 1.4 GHz. Note that our 1.4 GHz radio observations probe a typical rest-frame frequency of $\nu \sim 5$ GHz, for a source at the median AS2UDS redshift. Adopting the 16th or 84th percentile of our spectral index distribution for the K -correction (instead of $\alpha = -0.80$) leads to a typical difference of a factor of $1.5\times$ in the rest-frame 1.4 GHz radio luminosity. For SMGs without a radio counterpart, we adopt $4\times$ the local rms noise in the 1.4 GHz map and a fixed spectral index of $\alpha = -0.80$ in order to calculate the corresponding upper limit on the radio

¹⁸ The largest angular scale in the A-array, accounting for two-thirds of the observation time, equals $36''$, still significantly ($\sim 40\times$) larger than the typical radio sizes of SMGs.

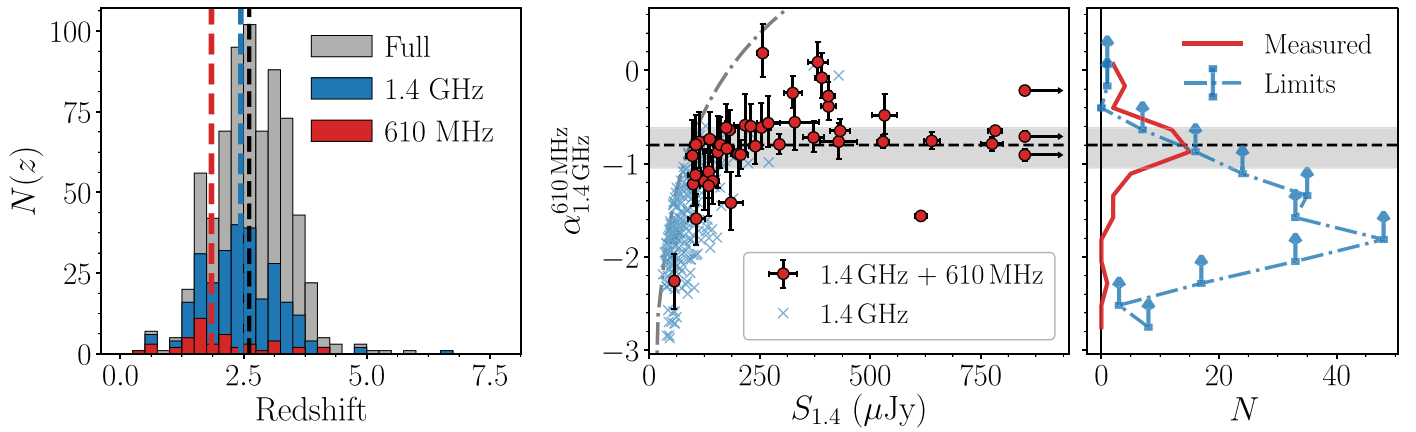


Figure 2. Left: distribution of the radio-detected AS2UDS population as a function of redshift. The full AS2UDS sample is shown, as are the subset detected at 1.4 GHz, and those sources detected at both 610 MHz and 1.4 GHz. The vertical, dashed lines show the median redshift of these three populations. The radio-detected subset lies at a slightly lower redshift than the full AS2UDS sample, as a result of the different K -corrections for the typical FIR- and radio-detected populations. Middle: radio spectral index as a function of the 1.4 GHz flux density. Sources with a 610 MHz detection, and hence with a measured spectral index, are highlighted. As expected, a large fraction of the lower limits on the spectral index corresponds to faint radio sources. The dashed-dotted line indicates the shallowest spectral index these sources can have in order to be detected at both 610 and 1400 MHz, assuming the central rms of $45 \mu\text{Jy beam}^{-1}$ at 610 MHz. For the limits, we adopt a fixed spectral index of $\alpha = -0.80$ (dashed horizontal line). This value lies well within the 1σ uncertainty on the stacked spectral index we find for AS2UDS subset detected at 1.4 GHz but not at 610 MHz (gray shaded region). Three sources with $S_{1.4} > 1 \text{ mJy}$ lie outside the plotting limits, and are shown as the arrows placed on the right. Right: distribution of spectral indices for the radio-detected AS2UDS sample, including direct measurements and lower limits. In this work, we mostly rely on a single radio detection at 1.4 GHz, and hence adopt a fixed spectral index for the majority of the radio-detected submillimeter galaxy sample.

luminosity. The FIR luminosities for the AS2UDS sample, obtained via MAGPHYS, are determined in the wavelength range $8\text{--}1000 \mu\text{m}$, and allow us to define the parameter q_{IR} characterizing the FIRRC. Following e.g., Condon et al. (1991b), Bell (2003), Magnelli et al. (2015), Calistro Rivera et al. (2017), we define it as

$$q_{\text{IR}} = \log_{10} \left(\frac{L_{\text{FIR}}}{3.75 \times 10^{12} \text{ W}} \right) - \log_{10} \left(\frac{L_{1.4}}{\text{W Hz}^{-1}} \right). \quad (2)$$

Here, the FIR luminosity L_{FIR} is normalized such that q_{IR} is dimensionless. For the full radio-detected subsample, we find a median $q_{\text{IR}} = 2.10 \pm 0.02$. Had we neglected the 610 MHz data and instead assumed a fixed spectral index of $\alpha = -0.80$, we would obtain a similar value of $q_{\text{IR}} = 2.11 \pm 0.02$. This value is lower than what is found for local, typically less strongly star-forming galaxies of $q_{\text{IR}} = 2.64 \pm 0.02$ (Bell 2003). However, it is similar to the values found by Kovács et al. (2006) and Magnelli et al. (2010) of respectively $q_{\text{IR}} = 2.07 \pm 0.09$ and $q_{\text{IR}} = 2.17 \pm 0.19$ for $z \approx 2$ radio-detected dusty star-forming galaxies, although other studies of SMGs find typical values for q_{IR} that are more similar to the local correlation (e.g., Ivison et al. 2010a; Sargent et al. 2010). We emphasize, however, that the average value of q_{IR} for any given sample is highly dependent on its selection, and the relative depths of the FIR and radio observations. Therefore, we compare with the results from the ALESS survey by Thomson et al. (2014) in more detail in Section 4.1, as both its submillimeter selection and radio coverage at 1.4 GHz are similar to that of AS2UDS.

In the following sections, we will study the FIRRC for two samples. First of all, we utilize all SMGs within the redshift range $1.5 \leq z \leq 4.0$, totaling 659 sources (93% of the entire AS2UDS sample). We limit ourselves to this redshift range to provide a more uniform selection of SMGs (Dudzevičiūtė et al. 2020), and will refer to this sample as the “full AS2UDS sample.” Second, we follow Dudzevičiūtė et al. (2020) and focus on the 133 SMGs at $1.5 \leq z \leq 4.0$ within the luminosity range $L_{\text{FIR}} = (4\text{--}7) \times 10^{12} L_{\odot}$ with at least one Herschel/SPIRE detection. By restricting ourselves to this luminosity range, we

ensure the sample is complete with respect to the SPIRE detection limits. As such, we retain a subsample complete in FIR luminosity, but with better constraints on its dust properties, due to the additional sampling of the FIR SEDs. Following Dudzevičiūtė et al. (2020), we will refer to this sample as the “luminosity-limited sample.”

3.2. AGNs in AS2UDS

A subset of our SMG sample exhibits strong radio emission causing them to be substantially offset from the FIRRC for purely star-forming galaxies (Figure 3). This excess in radio power is attributed to additional emission from an AGN in the center of the galaxy, and hence forms a contaminant for studies of the FIRRC. As a result, such radio-excess AGNs must be discarded from our sample, as it is not possible to disentangle the radio emission emanating from star formation or from the central AGN without resolving the radio emission, via, e.g., very long baseline interferometry (VLBI; e.g., Muxlow et al. 2005, 2020; Middelberg et al. 2013). Typically, radio-excess AGNs are seen to be hosted in red, passive galaxies (Smolčić 2009). Nevertheless, about 1% of local ultra-luminous infrared galaxies (ULIRGs) are also known to host such AGNs (Condon & Broderick 1986, 1991; Yun et al. 1999). Because our selection of SMGs does not involve their radio properties, it allows for an unbiased census of radio-excess AGNs in high-redshift, strongly star-forming galaxies, as compared to previous radio-selected studies.

We identify AGNs based on a fixed threshold of $q_{\text{IR}} \leq 1.55$, with sources below this threshold being defined as radio-excess AGNs (following, e.g., Del Moro et al. 2013). This value is chosen such that sources that are $\gtrsim 5\times$ radio-brighter compared to the median (stacked) FIRRC for the AS2UDS sample, as derived in Section 3.3, are identified as radio-excess AGNs. Our threshold is similar to the value of $q_{\text{IR}} = 1.70$ adopted by Thomson et al. (2014), but takes into account that our typical q_{IR} is slightly lower than that of their sample.

Upon adopting $q_{\text{IR}} = 1.55$ as our threshold, we find 12 radio-excess AGNs within the full AS2UDS sample (Figure 3), corresponding to a surface density of $\sim 12.5 \pm 3.6 \text{ deg}^{-2}$ at

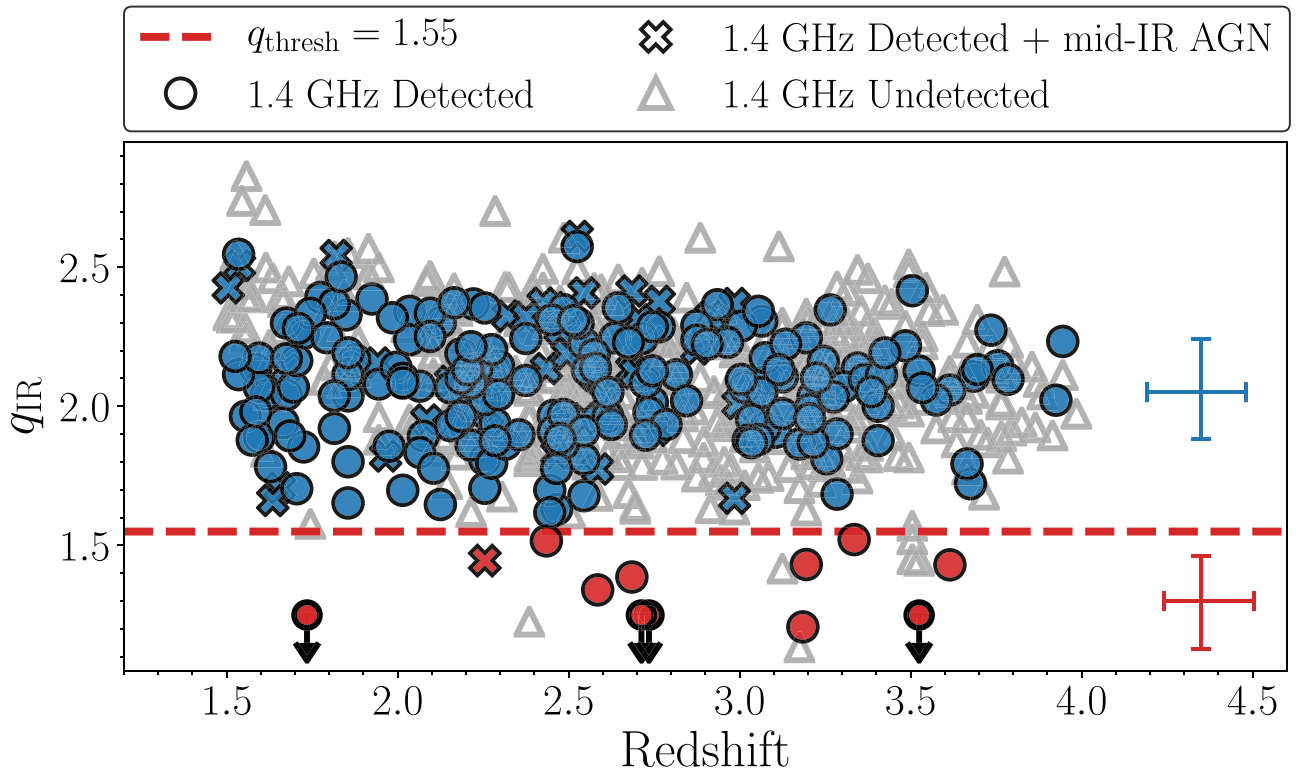


Figure 3. Distribution of q_{IR} as a function of redshift for the AS2UDS submillimeter galaxies (SMGs) within $1.5 \leq z \leq 4.0$. Galaxies with radio emission consistent with originating from star formation, defined as $q_{\text{IR}} > 1.55$ (red dashed line) are shown in blue, whereas radio-excess active galactic nuclei (AGNs) are shown in red. The plotting limits are chosen to focus on the cloud of star-forming sources around $q_{\text{IR}} \sim 2.1$, which cuts off four radio-excess AGNs within the range $q_{\text{IR}} = 0.35\text{--}0.95$. These are shown as red circles with downward-pointing arrows. We additionally show two representative errorbars for the radio-detected star-forming and AGN populations. Lower limits on q_{IR} are calculated using the corresponding upper limits on the SMG radio luminosity. Overall, AGNs make up only $1.8 \pm 0.5\%$ of the SMG population, and hence the radio emission of the majority of SMGs is consistent with originating from star formation.

$S_{870} \gtrsim 4$ mJy and $S_{1.4} \gtrsim 30 \mu\text{Jy beam}^{-1}$. Overall, $1.8 \pm 0.5\%$ of SMGs therefore hosts a radio-excess AGN, similar to what is observed in local ULIRGs (Condon & Broderick 1986, 1991; Yun et al. 1999). We have further investigated adopting other possible thresholds for identifying radio-excess sources, including using different cuts in q_{IR} , or adopting a redshift-dependent threshold in q_{IR} . The latter is commonly used for identifying AGNs in radio-selected samples (Calistro Rivera et al. 2017; Delhaize et al. 2017). However, we find that the FIRRC for AS2UDS is insensitive to the particular threshold we adopt, as the fraction of radio-excess AGNs we identify among our sample is small regardless. As such, we proceed with a threshold of $q_{\text{IR}} = 1.55$.

3.3. (A Lack of) Redshift Evolution in the FIRRC

In this section, we set out to constrain whether there is any redshift evolution in the FIRRC for the AS2UDS SMGs. In recent years, several studies have hinted at a decreasing value of q_{IR} at increasing redshift. However, these studies have mainly been based on radio-selected samples (e.g., Calistro Rivera et al. 2017; Delhaize et al. 2017) or optically selected samples (e.g., Magnelli et al. 2015). Thomson et al. (2014) carried out a study of the FIRRC based on a submillimeter-selected sample from the ALESS survey. However, with a modest sample of ~ 70 sources, Thomson et al. were unable to distinguish between a redshift-independent FIRRC, or one where q_{IR} decreases with redshift, as seen in radio-selected studies. With its tenfold increase in sample size, AS2UDS now

provides a set of SMGs numerous enough to distinguish between these possible scenarios.

Before we proceed, we address one potential limitation of our analysis, which is the lack of available spectral indices for the majority of our radio sample. It has recently been suggested that a simple power-law approximation for the radio spectrum of highly star-forming galaxies may be insufficient, and that in fact radio spectra may exhibit a spectral break around a rest-frame frequency of ~ 5 GHz (Thomson et al. 2019; Tisanić et al. 2019). For the full AS2UDS sample, where we probe rest-frame frequencies between $\nu_{\text{rest}} = 3.5\text{--}7$ GHz, any spectral steepening at high frequencies will affect the radio luminosities we calculate at rest-frame 1.4 GHz, which in turn will affect q_{IR} . A source at redshift z with a true spectral index α , for which a fixed value of $\alpha = -0.80$ was assumed, will have a calculated value of q_{IR} which is off by $\Delta q_{\text{IR}} = -(0.80 + \alpha) \times \log_{10}(1 + z)$, which amounts to approximately 0.2 dex at $z = 3$ for a spectral index equal to the 16th or 84th percentiles of our α_{1400}^{610} distribution. Any systematic variations in the radio spectral index with redshift will therefore induce—or potentially mask—evolution in the FIRRC.

To assess the extent to which such variations might affect the FIRRC for AS2UDS, we stack the full SMG sample—excluding radio AGNs, but including sources undetected at 1.4 GHz—in five distinct redshift bins, in both the 610 MHz and 1.4 GHz maps. We additionally stack in L_{FIR} and show the results in Figure 4. A linear fit through the data shows no evidence of spectral index evolution with either redshift or FIR luminosity, with a linear slope of -0.07 ± 0.16 and -0.15 ± 0.42 for the two parameters, respectively. The mean spectral indices are

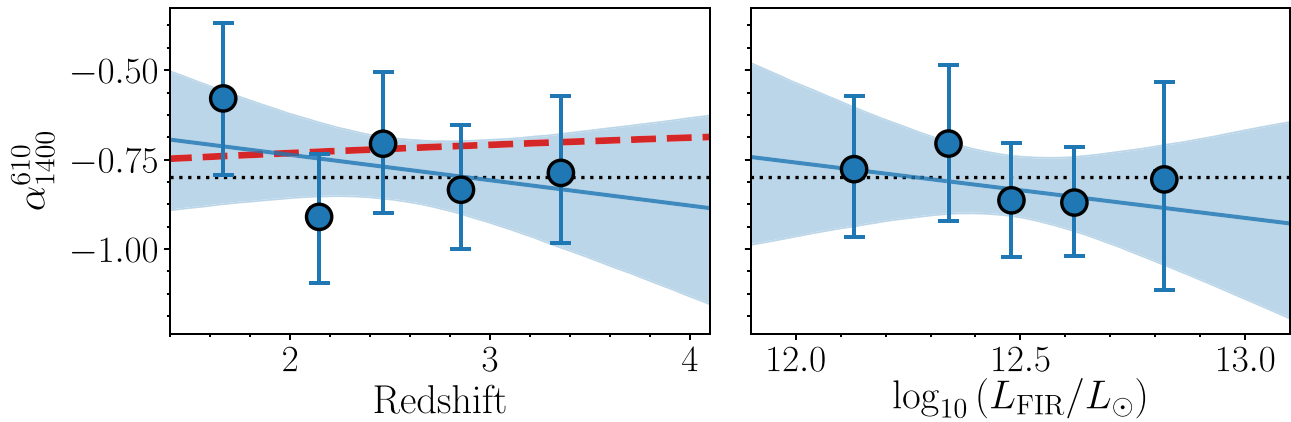


Figure 4. Spectral index between 610 MHz and 1.4 GHz for the full AS2UDS sample within $1.5 \leq z \leq 4.0$ (629 sources in total), computed for stacks in five bins in redshift (left) and FIR luminosity (right). The expected redshift evolution of the spectral index for an assumed synchrotron (free-free) spectral index of $\alpha = -0.85$ ($\alpha = -0.10$) and a thermal contribution of 10% at rest-frame 1.4 GHz is shown via the red dashed line in the left panel (e.g., Condon 1992). In both panels a linear fit is shown via the blue line, with the uncertainty shown through the shaded region. The fits are consistent with no gradient in both redshift and FIR luminosity, and hence adopting a fixed $\alpha = -0.80$ (black dotted line) does not affect our calculation of the FIR/radio correlation.

$\langle \alpha \rangle_z = -0.76 \pm 0.07$ for the redshift bins, and $\langle \alpha \rangle_{L_{\text{FIR}}} = -0.80 \pm 0.04$ for the stacks in FIR luminosity. Both values are consistent with a typical spectral slope of $\alpha = -0.80$, as well as with each other, within the uncertainties. We further compare our values with the evolution expected in the spectral index when assuming an increasing contribution of free-free emission at high redshift, as a result of probing higher rest-frame frequencies for these galaxies. For this, we assume the simple model for star-forming galaxies from Condon (1992), with a spectral index for synchrotron and free-free emission of, respectively, $\alpha_{\text{synch}} = -0.85$ and $\alpha_{\text{FF}} = -0.10$ (consistent with the values found by Niklas et al. 1997 and Murphy et al. 2011). The expected flattening of the 610–1400 MHz spectral index between $1.5 \leq z \leq 4.0$ is $\Delta\alpha \lesssim 0.1$, and we find no evidence for such modest evolution. This is fully consistent with Thomson et al. (2019), who in fact find a deficit in free-free emission for high-redshift SMGs. Overall, we find no significant variation in the 610–1400 MHz spectral index with either redshift or L_{FIR} , and we therefore conclude that the adopted radio spectral index is unlikely to be a driver of any trends in the AS2UDS FIRRC.

We now proceed by investigating any potential redshift evolution in the FIRRC for SMGs. In Figure 5 we show q_{IR} as a function of redshift for the full AS2UDS sample and the luminosity-limited sample. In both cases, we fit a function of the form $q_{\text{IR}}(z) \propto (1+z)^\gamma$ to *only* the SMGs detected at 1.4 GHz. As such, this sample is by construction biased toward radio-bright sources at higher redshift. For the full radio-detected AS2UDS sample, we find a lack of redshift evolution, with a best-fit solution of $\gamma_{\text{full}} = -0.01 \pm 0.03$. For the luminosity-limited sample, we do find an apparent evolution, and measure $\gamma_{\text{lum}} = -0.26 \pm 0.06$. However, this evolution is heavily driven by selection effects. While this sample is complete in FIR luminosity, the radio observations suffer from a positive K -correction, limiting the detection rate at high redshift. As a result, we are biased toward only the brightest radio sources at $z \gtrsim 3$. For a fixed range in L_{FIR} —which the luminosity-limited sample is by construction—radio-bright sources will have a low value of q_{IR} , and hence drive the average q_{IR} down at higher redshift.

While the lack of redshift evolution for the full radio-detected AS2UDS sample—which *still* is biased—is already interesting by itself, we need to address the radio-undetected population to get a proper census of any potential evolution of q_{IR} across redshift. We

do this by stacking the full and luminosity-limited samples in distinct redshift bins, having removed any radio AGNs. We show q_{IR} as a function of redshift for the stacked full and luminosity-limited samples in the bottom panels of Figure 5. Neither sample shows any evidence of variation with redshift, with the full sample following a trend given by $\gamma_{\text{full}} = 0.02 \pm 0.06$, and the luminosity-limited sample having a best fit of $\gamma_{\text{lum}} = -0.02 \pm 0.16$. For reference, we additionally show the 15 stacks and corresponding residuals of the full sample in Appendix A (Figure A3). We ensure the stacks are all of sufficient S/N ($\gtrsim 10$), such that reliable integrated flux measurements can be made, and any effects of noise boosting are minimal. As a result, the higher-redshift bins contain a larger number of sources than the low-redshift ones, to compensate for the negative radio K -correction. We verified however, that the results are not affected by the method of binning, and simply adopting bins with an equal number of sources gives consistent results in all cases.

From the stacked results we further obtain an average value of q_{IR} that, given our observed lack of redshift evolution, is representative for SMGs. For the full AS2UDS sample, we find a mean $q_{\text{IR,full}} = 2.20 \pm 0.03$, where the error represents the bootstrapped variation among the stacks. For the luminosity-limited sample, we find a similar value of $q_{\text{IR,lum}} = 2.26 \pm 0.02$, although across only five redshift bins. We further verify in Appendix A that the expected systematic uncertainty on these values, as a result of our reliance on a stacking analysis, is small, and amounts to $\Delta q_{\text{IR}} \lesssim 0.05$. As the typical values of q_{IR} for the full and luminosity-limited samples are consistent with one another, we will in the following investigate any possible trends between q_{IR} and other physical parameters for the full AS2UDS sample, as its radio and FIR properties match those of the luminosity-limited subsample. Interestingly, this typical q_{IR} for both samples is ~ 0.4 dex lower than the FIRRC observed locally (Bell 2003). We discuss this offset further in Section 4.2.

3.4. Correlations with Physical Properties

AS2UDS provides a large sample of SMGs for which Dudzevičiūtė et al. (2020) have derived various physical properties via MAGPHYS, such as stellar and dust masses, and star formation rates. In this section, we investigate if there is any variation in q_{IR} as a function of these parameters. In Figure 6 we show q_{IR} as a function of, respectively, L_{FIR} , star

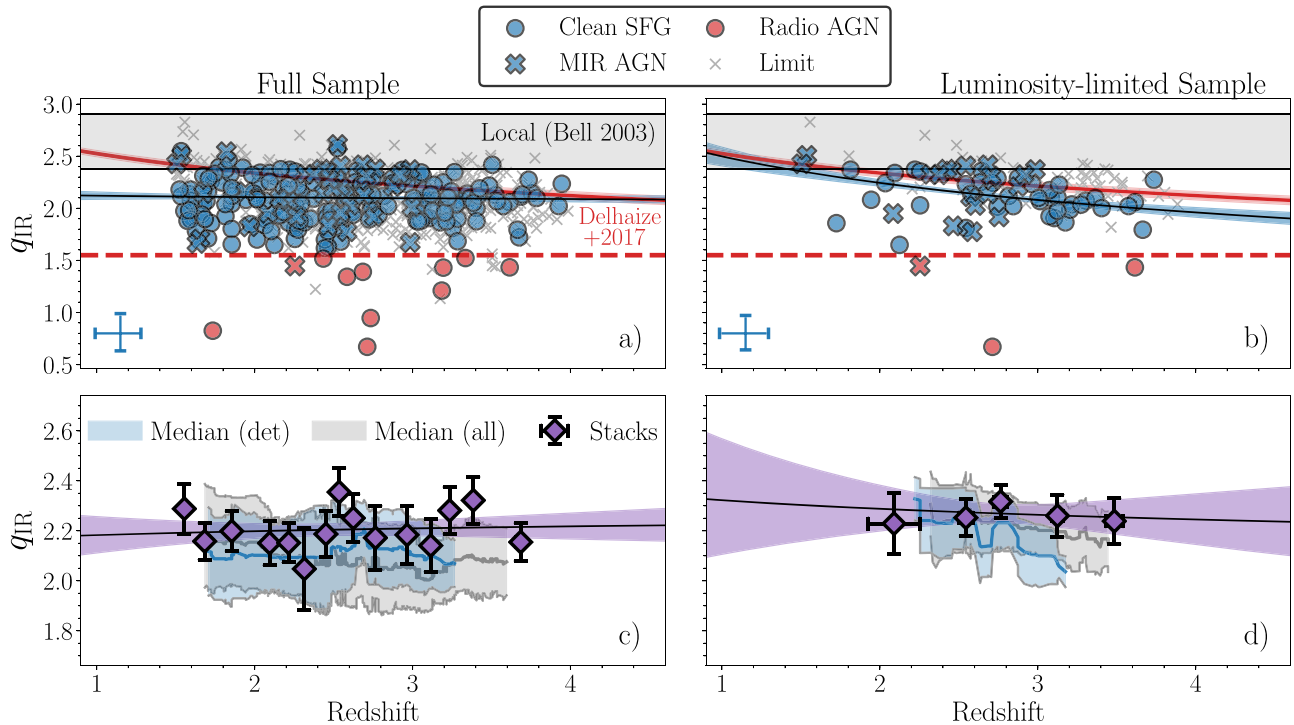


Figure 5. FIR/radio correlation (FIRRC) for AS2UDS as a function of redshift. (a) FIRRC for the full AS2UDS sample. The radio-detected star-forming sources are fitted by a power law of the form $q_{\text{IR}} \propto (1+z)^\gamma$. This fit and corresponding 1σ uncertainty are indicated via the black line and the blue shaded region. The FIRRC for the full radio-detected AS2UDS sample shows no hint of redshift evolution. For comparison, the local FIRRC and 1σ scatter from Bell (2003) is shown in the gray shaded band, and the evolving q_{IR} from Delhaize et al. (2017) is shown in red. A representative errorbar on q_{IR} is shown in the bottom left corner, and star-forming sources and AGNs are separated adopting a threshold of $q_{\text{IR}} = 1.55$ (dashed red line). (b) FIRRC for the radio-detected, luminosity-limited AS2UDS sample. In contrast to the full sample, this subset *does* show (artificial) evolution with redshift, as we select sources within a narrow range of L_{FIR} , but which are only sensitive to the brightest radio sources at the high-redshift tail of AS2UDS. (c) FIRRC for the full AS2UDS sample, based on stacking in the 1.4 GHz radio map in 15 distinct redshift bins. The black line and purple shaded region show a power-law fit through these points, and its corresponding confidence interval. The blue (gray) shaded region shows the running median through the radio detections (detections + nondetections), where the spread indicates the median absolute deviation. The stacked full AS2UDS sample shows no hint of redshift evolution. (d) Stacked FIRRC for the luminosity-limited AS2UDS sample. In contrast to the radio-detections only, the stacked luminosity-limited sample shows no redshift evolution in its FIRRC.

formation rate, M_* , M_{dust} , T_{dust} , and effective observed-frame $870\ \mu\text{m}$ -radius R_{eff} , the last of which was calculated for a subset of submillimeter-bright AS2UDS sources by Gullberg et al. (2019). In total, we have robust size measurements for 153 SMGs (70 are detected at 1.4 GHz). In order to assess the variation in q_{IR} in an unbiased way, we perform a stacking analysis by dividing our SMG sample into distinct bins for the aforementioned physical parameters, after the removal of radio AGNs.

The first panel shows q_{IR} as a function of IR luminosity. While the radio-detected subset of AS2UDS follows a weak positive trend, any correlation disappears when stacking. A linear fit through the stacked data points indicates a slope of $\beta = 0.16 \pm 0.10$, consistent with no evolution. Similarly, no correlation between q_{IR} and star formation rate exists (slope of $\beta = 0.07 \pm 0.10$), which is expected since L_{FIR} should be a good proxy for the star formation rate of SMGs.

Similarly, there does not appear to be any strong trend between q_{IR} and stellar mass, with a linear fit through the stacks being consistent with a slope of zero ($\beta = 0.07 \pm 0.06$). Likewise, there is no evidence for any trends between q_{IR} and either dust mass or temperature, with a slope of $\beta = -0.06 \pm 0.11$ and $\beta = (11 \pm 6) \times 10^{-3}$, respectively. Since no trend with dust luminosity exists, which is a combination of M_{dust} and T_{dust} , it is unsurprising that neither of these two parameters shows any trend with q_{IR} either. Finally, we show q_{IR} as a function of $870\ \mu\text{m}$ effective radius. As only a quarter of the full

AS2UDS sample has measured submillimeter radii, we employ a smaller number of bins to obtain sufficient S/N in each stack. Nevertheless, we see no hint of a trend between q_{IR} and R_{eff} , with a best-fitting linear slope of $\beta = 0.03 \pm 0.19$.

Overall, the AS2UDS SMGs do not appear to show any strong variation in q_{IR} as a function of their physical properties. None of the six parameters explored shows any hint of a correlation with q_{IR} at a 2σ or greater level. This may be the result of the relatively small dynamic range spanned by the sample, or may in fact imply that the FIRRC constitutes an especially robust correlation, even at high star formation rates and high redshift. We further discuss this in Section 4.2.

4. Discussion

4.1. Previous Studies of the FIRRC

Neither the full AS2UDS sample, nor its radio-detected subset, shows any evidence for evolution in their FIRRCs. In this section, we compare this lack of evolution with previous studies, including radio-based ones, which typically have large sample sizes, and SMG-based ones, having selection criteria that are more similar to ours.

Recently, the FIRRC has been studied by Delhaize et al. (2017) for the 3 GHz-selected VLA-COSMOS sample (Smolčić et al. 2017a, 2017b). They utilize a sample of nearly 10,000 star-forming galaxies at a median redshift of $z \sim 1.0$, and employ a survival analysis to attempt to account for nondetections at either radio or

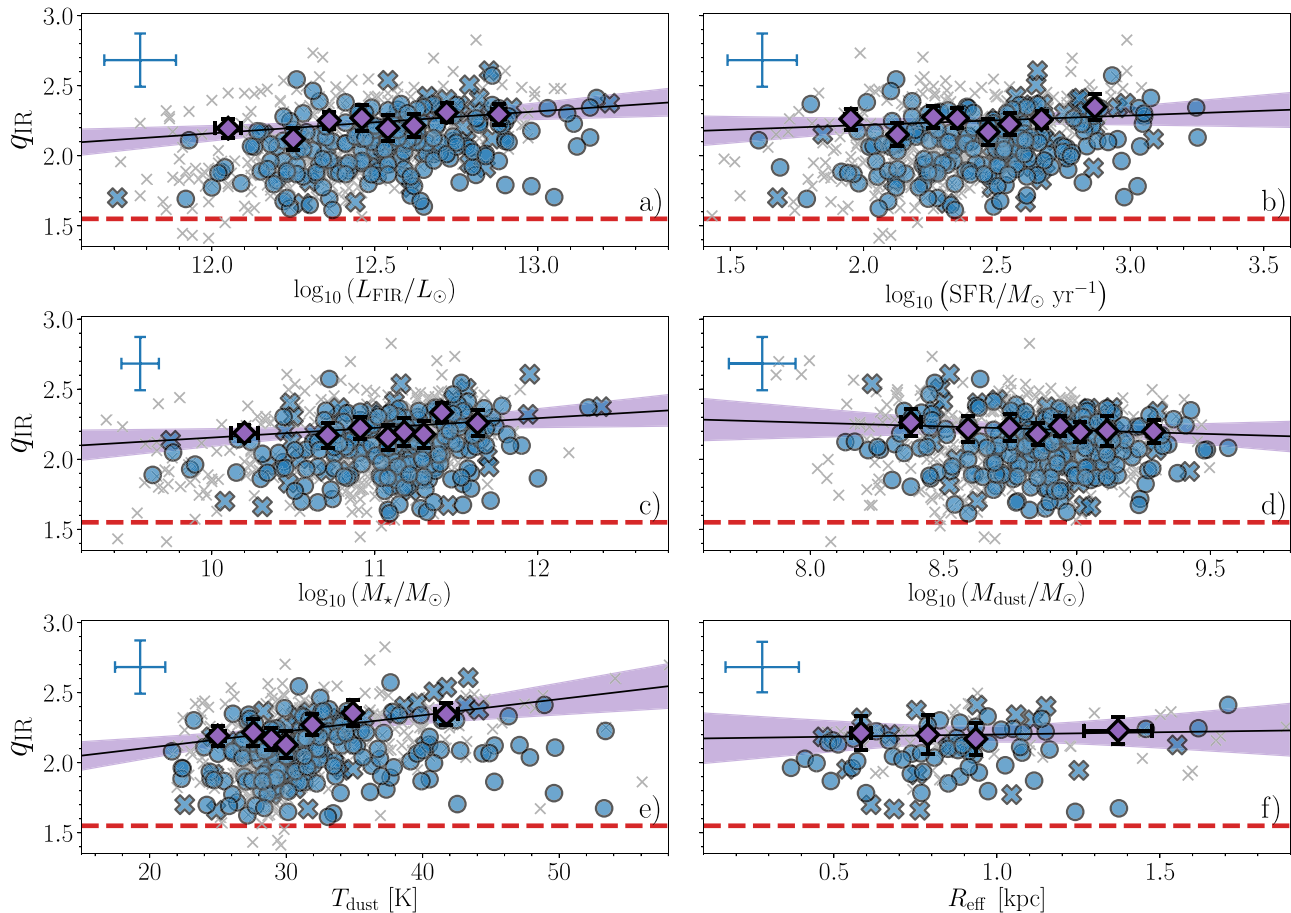


Figure 6. FIRRC parameter q_{IR} as a function of several physical parameters for the full AS2UDS sample, after removal of radio-excess AGNs. In all panels, we show radio-detected SMGs as blue circles (or blue crosses, when they show a mid-IR AGN signature). A representative uncertainty for these is shown in the upper left corner of each panel. Lower limits on q_{IR} are shown as gray crosses. The stacks are plotted as purple diamonds, with a linear fit to the stacks shown via the black line. The purple shaded region indicates the corresponding 16th–84th percentile confidence region on the fit. (a) q_{IR} as a function of FIR luminosity. (b) q_{IR} as a function of star formation rate. (c) q_{IR} as a function of stellar mass. (d) q_{IR} as a function of dust mass. (e) q_{IR} as a function of dust temperature. (f) q_{IR} as a function of effective radius for sources with a robust submillimeter size measurement from Gullberg et al. (2019). None of the panels show any significant trends between q_{IR} and the various physical parameters at a $\geq 2\sigma$ level.

FIR wavelengths. They find statistically significant redshift evolution of the FIRRC, with a slope of $\gamma_{\text{D17}} = -0.19 \pm 0.01$, out to $z \sim 3$. Molnár et al. (2018) extend this study by further tying in rest-frame UV morphological information for a subset of ~ 4700 sources out to $z \sim 1.5$. They split their sample into disk- and spheroid-dominated galaxies, and find that while the FIRRC for the latter shows significant redshift evolution, similar to the study by Delhaize et al. (2017), the disk-dominated galaxies show minimal evolution, with a slope of $\gamma_{\text{M18}} = -0.037 \pm 0.012$. As radio AGNs are typically found in red, bulge-dominated galaxies (e.g., Smolčić 2009), this difference between the two samples is interpreted by Molnár et al. (2018) as residual AGN contamination in spheroidal galaxies, and they argue the “true” FIRRC shows no evolution out to $z \sim 1.5$.

The FIRRC was additionally studied at 1.4 GHz for a different radio sample by Calistro Rivera et al. (2017), using Westerbork Synthesis Radio Telescope observations over the Boötes field. They include upper limits at both FIR and radio wavelengths using forced photometry, for a total of ~ 800 sources. They too find significant redshift evolution in the FIRRC at 1.4 GHz, out to $z \lesssim 2.5$, with a slope of $\gamma_{\text{CR17}} = -0.15 \pm 0.03$, consistent with the aforementioned results from Delhaize et al. (2017).

Radio-selected samples, however, are by definition sensitive to radio-bright sources, and hence by construction select based

on the combined radio luminosity from star formation and AGN activity. FIR-based surveys, in this regard, are mostly sensitive to emission solely from star formation activity, as emission from a warm AGN torus is typically confined to mid-IR wavelengths (e.g., Lyu & Rieke 2017; Xu et al. 2020). To substantiate this, we show in Appendix B that radio AGNs are a factor of ~ 5 more prevalent in radio-selected samples than in AS2UDS, at matched flux densities. As such, FIR-selected samples are expected to be substantially less contaminated by AGNs.

For this reason, we now turn to two IR-based studies of the FIRRC. We stress, however, that these typically have smaller sample sizes compared to radio-based surveys, but are less likely to suffer AGN contamination. Ivison et al. (2010b) investigated the FIRRC out to $z \sim 2$ using a Herschel $250 \mu\text{m}$ selected sample over the GOODS-North field. They find modest evolution of $\gamma_{\text{I10}} = -0.26 \pm 0.07$ for a FIR-detected sample with $L_{\text{FIR}} = 10^{11} - 10^{12} L_{\odot}$, though their study is potentially affected by the large Herschel point-spread function and lack of high-resolution $250 \mu\text{m}$ identifications, complicating the association of radio counterparts to FIR detections, and additionally complicating any stacking analyses.

These problems were overcome by Thomson et al. (2014), who investigated the FIRRC for the ALESS $870 \mu\text{m}$ sample.

Their sample selection is similar to that of AS2UDS, constituting an ALMA interferometric follow-up of submillimeter sources initially detected at the same wavelength in a single-dish survey (Hodge et al. 2013; Karim et al. 2013). The depth of both the ALESS and AS2UDS parent surveys and follow-up ALMA observations are roughly similar, as are the noise levels of the 1.4 GHz radio maps over the ECDFS and UDS fields, with the main difference being survey area and hence sample size. Therefore, ALESS forms the natural comparison sample to AS2UDS, and as such we compare the two surveys in additional detail.

Thomson et al. (2014) individually detect 52 SMGs at 1.4 GHz, out of a parent SMG sample of 76 galaxies. We note that this parent sample excludes 21 SMGs that are optically faint, and hence had no reliable photometric redshift available (see also Simpson et al. 2014). For the radio-detected subsample, Thomson et al. (2014) find no evidence of redshift evolution in the FIRRC, with a fitted slope of $\gamma_{T14} = -0.15 \pm 0.17$. Upon further including radio-undetected sources via a stacking analysis, they find a typical q_{IR} across the full ALESS sample of $q_{\text{IR}} = 2.35 \pm 0.04$.¹⁹ When limiting ourselves to the SMGs at $z \geq 1.5$ that do not exhibit a radio-excess signature, similar to our approach for AS2UDS, the ALESS sample shows a typical value of $q_{\text{IR}} = 2.33 \pm 0.04$. This is roughly similar to the typical value for AS2UDS of $q_{\text{IR}} = 2.20 \pm 0.03$. The small remaining difference of ~ 0.1 dex is likely the result of the slightly deeper SCUBA-2 map (typical rms of $\sigma = 0.9 \mu\text{Jy beam}^{-1}$; Geach et al. 2017; Stach et al. 2019) compared to the LESS parent survey for ALESS ($\sigma = 1.2 \mu\text{Jy beam}^{-1}$; Hodge et al. 2013). Similarly, the AS2UDS ALMA observations are deeper than their ALESS counterparts. As a result, AS2UDS will identify somewhat IR-fainter galaxies, which will decrease the typical q_{IR} of the sample. We further note that Thomson et al. (2019) study the FIRRC for a subset of 38 AS2UDS sources detected at both 1.4 and 6 GHz, for which they find a typical $q_{\text{IR},T19} = 2.20 \pm 0.06$, consistent with the typical q_{IR} we derive for the full AS2UDS sample.

Overall, while redshift evolution of the FIRRC is near-unanimously found in radio surveys, evidence for such evolution when starting from IR-selected samples is only weak. Both this observation and the aforementioned results from Molnár et al. (2018) point toward unidentified radio AGNs being the root cause of artificial evolution in the FIRRC in radio-selected surveys. However, we show in Appendix C, based on a combination of low-resolution radio and VLBI observations in the COSMOS field, that this bias is insufficient. Summarizing, the VLBI data are predominantly sensitive to radio AGN; however, the total radio emission in these high-resolution observations is not sufficient to explain the AGN contamination required in order to generate an evolving FIRRC, when compared to the total radio emission observed in the lower-resolution VLA radio observations.

4.2. The FIRRC for SMGs

Observations of SMGs at high redshift have suggested that these systems are typically radio-bright compared to the local FIRRC (e.g., Kovács et al. 2006; Murphy et al. 2009; Magnelli et al. 2010), though a clear demonstration of this offset has until now been complicated by the mostly small sample sizes

employed, and their reliance on incomplete, radio-detected subsamples. For just the radio-detected AS2UDS SMGs, we find a typical $q_{\text{IR}} = 2.10 \pm 0.02$ (scatter $\sigma_q = 0.21 \text{ dex}$ ²⁰), which is indeed substantially offset from the local correlation ($q_{\text{IR}} = 2.64$ with a scatter of 0.26 dex; Bell 2003). However, this median value for AS2UDS is biased toward radio-bright sources as a result of selection. A truly representative value of q_{IR} is obtained through our stacking analysis, which indicates a typical $q_{\text{IR}} = 2.20 \pm 0.03$. This implies that, even after correcting for selection effects, the FIRRC for our AS2UDS SMGs is offset from the local correlation for star-forming galaxies by $0.44 \pm 0.04 \text{ dex}$ (a factor of 2.8 ± 0.2), while not showing any evidence for redshift evolution between $1.5 \leq z \leq 4.0$ (a 3σ upper limit of $\leq 0.08 \text{ dex}$ across this $\sim 3 \text{ Gyr}$ period). Consequently, this substantiates the finding of SMGs being radio-brighter relative to their FIR luminosity compared to normal, star-forming galaxies found locally.

The most straightforward explanation for this offset would be the contribution from an AGN to the observed radio emission. Based on the 0.4 dex offset from the local FIRRC, this requires the AGN to contribute $\sim 70\%$ of the total radio luminosity. However, the small amount of scatter we observe around the correlation, as well as the low fraction of radio-excess AGNs, requires substantial fine-tuning of AGN luminosities. VLBI observations further indicate a modest incidence of radio-excess AGNs, with three out of 11 SMGs in the literature showing evidence for a compact core, indicative of an AGN (based on the combined samples of Biggs et al. 2010, Momjian et al. 2010, and Chen et al. 2020). These samples, in turn, explicitly target radio-bright SMGs, and the bright radio population is known to be dominated by radio-excess AGNs (e.g., Condon 1989). As such, the incidence of dominant radio AGNs in SMGs is likely to be a lot smaller than the $\sim 30\%$ indicated by these VLBI studies.

Instead, both the offset in the FIRRC, and the lack of redshift-evolution for SMGs, are likely to be indicative of the different physics at play in normal, low-luminosity star-forming galaxies observed locally, and the much more active systems being studied at high redshift.

The calorimetric models of the FIRRC indeed make predictions for variations in the FIRRC as a function of star formation surface density (Lacki et al. 2010), which may explain the difference between SMGs and the normal star-forming population. In addition, Lacki & Thompson model the behavior of the FIRRC at high redshift, for galaxies with a variety of star formation surface densities. With our large, homogeneous sample of SMGs, we can investigate the predictions of these models in detail. In the next section, we compare the FIRRC of the AS2UDS SMGs with that of normal star-forming galaxies. In Section 4.2.2, we focus on the comparison with ULIRGs, thought to be the closest local analogs of $z \sim 2$ dusty star-forming galaxies.

4.2.1. SMGs Compared to Normal Star-forming Galaxies

Given that our low-frequency radio observations predominantly probe nonthermal synchrotron emission originating from relativistic electrons, we first discuss the FIRRC in terms of the various physical processes that compete for these electrons. In theory, the correlation is expected to break down at high redshift due to the increased inverse Compton losses of cosmic

¹⁹ This is ~ 0.2 dex lower than was quoted in Thomson et al. (2014) (A. Thomson 2020, private communication).

²⁰ This scatter is likely predominantly driven by the propagated measurement error on q_{IR} , which averages 0.18 dex.

rays on the CMB (e.g., Murphy 2009; Lacki & Thompson 2010; Schleicher & Beck 2013). Under the assumption that synchrotron and inverse Compton are the dominant processes of energy loss, a star-forming galaxy with a magnetic field of $B = 10 \mu\text{G}$, as is typical for local, normal star-forming galaxies (Beck & Wielebinski 2013; Tabatabaei et al. 2017), is expected to show an increased q_{IR} at $z = 4$ compared to the local value of $\Delta q_{\text{IR}} \simeq 1.0$ dex, as a result of the warmer CMB at high redshift. Highly star-forming galaxies, however, are the most resilient to this, as their star formation-powered radiation fields are substantially stronger than the CMB, even at moderate redshift. Under the assumption that our SMGs represent central starbursts with typical radius of 1 kpc (e.g., Gullberg et al. 2019), the energy density U_{rad} of their star formation-powered radiation field is still an order of magnitude higher than that of the CMB at $z = 3$. The two energy densities are only expected to coincide at $z \sim 6$, and due to the steep redshift dependence of inverse Compton losses on the CMB ($U_{\text{CMB}} \propto (1+z)^4$, e.g., Murphy 2009), such losses are negligible for the typical redshift range covered by SMGs. As such, no evolution in the FIRRC is expected for the AS2UDS sample as a result of the warmer CMB at high redshift.

As we find the FIRRC for SMGs to constitute a particularly tight correlation, the relative radiative losses to synchrotron, inverse Compton, and other potential sources of energy loss, such as ionization losses and bremsstrahlung (see, e.g., Thompson et al. 2006; Murphy 2009; Lacki et al. 2010), have to be relatively constant across our sample (and hence across redshift). This, too, is not surprising. We find no significant variation in q_{IR} with a variety of physical parameters (Section 3.4), either for the individually radio-detected sources, or for the stacks. Dudzevičiūtė et al. (2020) further investigated any redshift evolution for a variety of physical properties of the AS2UDS SMGs, and found only a strong increase in typical star formation rates with increasing redshift. Further evolution in, e.g., dust masses or gas fractions is only modest, and typically less than the differential evolution observed for the UDS field population. Overall, this paints the picture of SMGs as a fairly homogeneous galaxy population across redshift. Using a simple analytic model, Dudzevičiūtė et al. (2020) explain the redshift distribution of SMGs as the combination of systems growing through a characteristic halo mass ($M_h \sim 4 \times 10^{12} M_\odot$) and acquiring a certain minimal gas fraction. If this threshold is associated with starburst activity, the SMG population might consist of physically similar galaxies, simply observed at different cosmic epochs. As radiative losses on the CMB remain negligible for our SMGs, as a result of the high star formation-powered radiation fields, the lack of redshift evolution in the FIRRC of SMGs may simply be a consequence of their homogeneity.

This lack of evolution, however, does not explain the intrinsic offset of SMGs with respect to the local FIRRC. Lacki et al. (2010) argue that this offset is likely the result of the enhanced magnetic fields in SMGs, compared to those of the normal star-forming population. Neglecting, for now, other potential sources of cosmic ray energy loss besides inverse Compton, the fact that SMGs obey the FIRRC implies that $U_{\text{B}}/U_{\text{rad}} \gtrsim 1$ (Murphy 2009), where $U_{\text{B}} = B^2/8\pi$. In other words, synchrotron emission must dominate the energy loss of cosmic rays, and the ratio of synchrotron to inverse Compton losses has to be relatively constant in general to explain the small scatter about the FIRRC. This, in turn, implies a minimum magnetic field strength for

SMGs of $B_{\text{min}} \gtrsim 0.1\text{--}0.2$ mG. Such magnetic fields are indeed expected for SMGs (Thompson et al. 2006; Murphy 2009), and are additionally in agreement with the B -star formation rate relation deduced for local, normal star-forming galaxies by Tabatabaei et al. (2017), though we caution this requires an extrapolation across nearly two orders of magnitude in star formation rate.

If ionization losses and bremsstrahlung are additionally expected to become important in highly star-forming galaxies, synchrotron emission has to be even stronger to maintain the FIRRC. In particular, enhanced synchrotron emission in SMGs is expected, as a result of their strong magnetic fields and what Lacki et al. (2010) call the “ ν_c -effect”: a cosmic ray electron with an energy E will predominantly emit synchrotron radiation at a frequency ν_c , which is given by (e.g., Murphy 2009)

$$\left(\frac{\nu_c}{\text{GHz}}\right) = 1.3 \times \left(\frac{B}{0.1 \text{ mG}}\right) \left(\frac{E}{\text{GeV}}\right)^2. \quad (3)$$

Hence, at a greater magnetic field strength, observations at a fixed frequency will probe lower-energy electrons. The distribution of injected electrons typically follows a power-law distribution in energy, $N(E) \propto E^{-p}$, where p relates to the observed radio spectral index via $p = -(\alpha - 1)$, in the absence of cooling. Typical values are $p > 2$, and in particular with $\alpha \approx -0.80$ we obtain $p \approx 2.6$. This, in turn, implies that the lower typical energy of the electrons we probe is more than compensated for by them being substantially more numerous than their high-energy counterparts. This will, then, enhance the radio emission seen in SMGs. In particular, Lacki et al. (2010) propose that $q_{\text{IR}} \propto \left(1 - \frac{1}{2}p\right) \log_{10} B$. If we assume the offset of SMGs with respect to the local FIRRC is solely the effect of stronger magnetic fields in SMGs and the resulting ν_c -effect, our observed $p = 2.6$ implies SMGs have magnetic field strengths about 20 times larger than for typical local galaxies. As these generally have magnetic fields of $B \sim 10 \mu\text{G}$ (e.g., Tabatabaei et al. 2017), this implies that SMGs likely have magnetic fields of $B \sim 0.2$ mG, consistent with our previous minimum requirement on the field strength to maintain a linear FIRRC. While such magnetic fields are indeed strong compared to local, normal star-forming sources, they are smaller than the typical ~ 1 mG fields observed in local ULIRGs (Robishaw et al. 2008; McBride et al. 2014). Arp220, in particular, has an estimated magnetic field strength of $B \approx 2$ mG (McBride et al. 2015; Yoast-Hull et al. 2016). This difference is potentially due to ULIRGs being substantially more compact than SMGs, having similar levels of star formation in volumes of a few hundred parsecs (Solomon et al. 1997; Downes & Solomon 1998), instead of the approximately kiloparsec scales that are typical for SMGs (Simpson et al. 2015; Hodge et al. 2016; Gullberg et al. 2019). We compare the FIRRC for SMGs and ULIRGs in more detail in Section 4.2.2.

While seemingly satisfactory, simply enhancing the magnetic field of SMGs with respect to normal star-forming galaxies raises another issue, as was already noted by Thompson et al. (2006). The synchrotron cooling time is proportional to $B^{-3/2}$ (Murphy 2009), and hence large magnetic field strengths imply very short synchrotron cooling times. This spectral aging should in principle be observable in the synchrotron spectrum, manifesting itself as a spectral break. Such spectral features have indeed been claimed in the radio spectra of SMGs (e.g., Thomson et al. 2019), at frequencies $\nu_b \gtrsim 5$ GHz. For a single injection event of cosmic rays, subject to a magnetic field B , a

spectral break arises at frequency ν_b after a time τ_b , which is given by (Carilli & Barthel 1996)

$$\tau_b = 1.6 \times \left(\frac{B}{0.1 \text{ mG}} \right)^{-3/2} \left(\frac{\nu_b}{\text{GHz}} \right)^{-1/2} \text{ Myr.} \quad (4)$$

For a single short burst of star formation, a spectral break at 5 GHz implies the synchrotron emission must have arisen within the last megayear, assuming $B = 0.2 \text{ mG}$.²¹ Additionally, for a top-hat star formation history, modeled as a succession of single injection events following Thomson et al. (2019), the 610–1400 MHz spectral index should have steepened to $\alpha \approx -1.2$ after only 20 Myr, with only minor differences when either a linearly rising, or exponentially declining star formation history is assumed instead. Even accounting for the fact that synchrotron emission will lag the onset of the starburst by $\sim 30 \text{ Myr}$ (Bressan et al. 2002), this is still inconsistent with the expected typical age of our SMGs of $\sim 150 \text{ Myr}$, based on an analysis of depletion timescales (Dudzevičiūtė et al. 2020).

At more realistic starburst timescales, the spectral break should manifest at much lower frequencies, and hence the 610–1400 MHz spectral index should be considerably steeper than the observed $\alpha \approx -0.8$. Thompson et al. (2006) argue that, in the dense starburst environments, bremsstrahlung and ionization form additional sources of energy loss of cosmic ray electrons. Ionization losses, in particular, are most effective for low-energy cosmic rays, and hence will flatten the observed radio spectrum. For the cooling times for inverse Compton emission and ionization losses (respectively Equations (4) and (10) in Murphy 2009) to be equal, given a magnetic field of 0.1 mG (1 mG), requires an ISM density of $n_{\text{ISM}} \sim 10^3 \text{ cm}^{-3}$ ($n_{\text{ISM}} \sim 10^2 \text{ cm}^{-3}$). That is, for larger densities, ionization losses will dominate over inverse Compton cooling. Such densities are typical for the central regions of SMGs (e.g., Bothwell et al. 2013; Rybak et al. 2019), and hence the spectral steepening can be counteracted via ionization losses. In the models of Thompson et al. (2006) and Lacki & Thompson (2010), this indeed results in an expected $\alpha \approx -0.80$ at the rest-frame frequencies we probe for the AS2UDS SMGs, which is consistent with our observations.

However, if ionization cooling is additionally important in SMGs, it will compete with synchrotron emission for the available cosmic rays. In particular, increased ionization losses should work to reduce the observed synchrotron emission by a factor of ~ 2 ($\Delta q_{\text{IR}} \approx +0.3 \text{ dex}$; Thompson et al. 2006), which in turn partially compensates for the offset in the FIRRC as a result of the stronger magnetic fields in SMGs. To alleviate this tension, Lacki et al. (2010) suggest that the production of secondary cosmic ray electrons and positrons, resulting from proton–proton collisions in the high-density environment of a starburst galaxy, are generating additional synchrotron emission. Indeed, their models including the creation of secondary cosmic rays show a decrease of $\Delta q_{\text{IR}} \approx -0.4 \text{ dex}$ at SMG-like gas surface densities, compared to models with only primary cosmic rays, which offsets the additional energy loss from bremsstrahlung and ionization losses. In particular, the creation of secondary cosmic rays should counteract strong spectral index gradients in galaxies hosting a central starburst, as these can be generated also outside the star-forming regions. While

testing this at high redshift is currently only possible in strongly gravitationally lensed galaxies (e.g., Thomson et al. 2015), resolved multifrequency observations of Arp220 between 150 MHz and 33 GHz indicate that cosmic ray electrons are required to be accelerated far outside the central regions in order to explain the spectral index maps (Varenius et al. 2016), providing support to the importance of secondary cosmic rays (see also the discussion of multifrequency source sizes in Thomson et al. 2019).

Overall, our favored explanation for the lack of evolution in the FIRRC for SMGs, as well as its offset from the local value for normal star-forming galaxies, involves a fair amount of fine-tuning. Summarizing, it requires (i) strong magnetic fields ($B \gtrsim 0.1\text{--}0.2 \text{ mG}$) to explain the offset in the FIRRC, (ii) significant ionization losses to counteract spectral aging and flatten the observed radio spectra, and (iii) secondary cosmic rays to compensate for this additional energy loss through ionization. This “conspiracy” indeed forms the basis for the models by Lacki et al. (2010) and Lacki & Thompson (2010) in order to maintain a linear FIRRC across a wide range of FIR and radio luminosities. To test this scenario in more detail, ideally resolved radio and FIR observations of a sizeable sample of SMGs are required. However, unresolved observations may be able to shed some light on the physical processes as well. The magnetic field strength of a galaxy likely depends on its star formation activity, either through the gas surface or volume density and the Kennicutt–Schmidt relation (Lacki et al. 2010; Lacki & Thompson 2010), or directly via the observed star formation rate (Tabatabaei et al. 2017). If this correlation is continuous, one expects to see a negative correlation between q_{IR} and star formation rate, across a wide range from normal star-forming galaxies down to SMGs.

If such a trend indeed exists, this will have a significant effect on studies of the FIRRC that are not uniformly sensitive to star formation across redshift. In particular, we argued in Section 4.1, and return to in Appendix C, that radio AGNs alone cannot explain the observed redshift evolution in radio-selected studies of the FIRRC. As such, it is probable that this evolution is instead the result of probing different galaxy populations locally and at high redshift. Unlike in the case of our FIR-selected sample, selection at radio wavelengths is subject to a positive K -correction, such that at high redshift one is only sensitive to strongly star-forming galaxies (e.g., Condon 1992). In addition, the average high-redshift galaxy is more rapidly forming stars than a typical local star-forming galaxy (e.g., Speagle et al. 2014). As such, radio-based studies will probe more “SMG-like” galaxies at high redshift, which implies that the average q_{IR} probed should reflect the lower normalization for the FIRRC of SMGs. In turn, this should induce redshift evolution in the FIRRC, similar to what is observed (Calistro Rivera et al. 2017; Delhaize et al. 2017). The evolving q_{IR} adopted in recent radio-based studies of the cosmic star formation rate density (e.g., Novak et al. 2017; Ocran et al. 2020) should therefore be appropriate, as this quantity encompasses the modified conversion from radio emission to star formation rate when considering different galaxy populations.

Testing this scenario, however, will require a star-forming sample with a fixed range of star formation rates across redshift, where the star formation rate is measured using a preferably dust-unbiased tracer independent of FIR and synchrotron emission. The most obvious candidates for this

²¹ Given that we observe no deviations from a fixed spectral index of $\alpha = -0.80$ —typical for uncooled synchrotron emission—out to $z \approx 4.0$, if a break exists, it is likely to lie at $\nu_b > 5 \text{ GHz}$, which will further decrease τ_b .

will be radio free–free emission and [C II] 158 μm emission, both of which suffer little from dust attenuation, and may provide an effective means of studying the FIRRC without requiring expensive, resolved FIR and radio observations.

4.2.2. SMGs Compared to Local ULIRGs

The discussion in the previous section focused primarily on the difference in the FIRRC between SMGs and local, normal star-forming galaxies. However, ULIRGs potentially constitute the closest local analogues of $z \sim 2.5$ SMGs. They show FIR luminosities in excess of $10^{12} L_{\odot}$, and their typical magnetic field reaches milliGauss strengths (Robishaw et al. 2008; McBride et al. 2014, 2015; Yoast-Hull et al. 2016), substantially larger than that of normal galaxies. However, ULIRGs *do* fall onto the local FIRRC (Yun et al. 2001; Farrah et al. 2003; Jarvis et al. 2010; Galvin et al. 2018). If ULIRGs are indeed close analogs of SMGs, and magnetic fields are the primary driver of their different FIRRC, this raises the question of why these seemingly similar galaxy populations are offset in q_{IR} by ~ 0.4 dex.

While a detailed investigation of this offset is beyond the scope of this paper, we can afford to be more quantitative in a comparison between ULIRGs and SMGs. In the following, we will assume that all star formation is dust-obscured in both populations, and that the same physical processes for cosmic ray energy loss dominate. In particular, the strong magnetic fields and high densities present in both ULIRGs and SMGs indicate that the dominant processes are synchrotron, inverse Compton, ionization, and bremsstrahlung. Their cooling times are given in Murphy (2009), and are reproduced here:

$$\begin{aligned} \left(\frac{\tau_{\text{syn}}}{\text{yr}}\right) &\approx 4.4 \times 10^4 \left(\frac{\nu}{\text{GHz}}\right)^{-1/2} \left(\frac{B}{\text{mG}}\right)^{-3/2} \\ \left(\frac{\tau_{\text{IC}}}{\text{yr}}\right) &\approx 1.6 \times 10^6 \left(\frac{\nu}{\text{GHz}}\right)^{-1/2} \left(\frac{B}{\text{mG}}\right)^{1/2} \\ &\quad \times \left(\frac{L_{\text{bol}}}{10^{12} L_{\odot}}\right)^{-1} \left(\frac{R}{\text{kpc}}\right)^2 \\ \left(\frac{\tau_{\text{ion}}}{\text{yr}}\right) &\approx 1.1 \times 10^9 \left(\frac{\nu}{\text{GHz}}\right)^{1/2} \left(\frac{B}{\text{mG}}\right)^{-1/2} \left(\frac{n_{\text{ISM}}}{\text{cm}^{-3}}\right)^{-1} \\ &\quad \times \left(\frac{3}{2} \left[\ln\left(\frac{\nu}{\text{GHz}}\right) - \ln\left(\frac{B}{\text{mG}}\right)\right] + 39\right)^{-1} \\ \left(\frac{\tau_{\text{brem}}}{\text{yr}}\right) &\approx 8.7 \times 10^7 \left(\frac{n_{\text{ISM}}}{\text{cm}^{-3}}\right)^{-1}. \end{aligned} \quad (5)$$

Here L_{bol} is the bolometric luminosity of the galaxy, assumed to equal the 8–1000 μm luminosity, and n_{ISM} is the particle number density of the ISM. The fraction of cosmic ray energy that is emitted via synchrotron radiation can then be written as

$$f_{\text{syn}} = \frac{1/\tau_{\text{syn}}}{\sum_{\text{proc}, i} 1/\tau_i}, \quad (6)$$

where the sum iterates over all cooling timescales in Equation (5). Crucially, f_{syn} will depend on the frequency probed, as the various cooling timescales in Equation (5), with the exception of bremsstrahlung, all contain a frequency dependence. Synchrotron and inverse Compton losses are stronger at higher frequencies, as

Table 1
Benchmark Models for ULIRGs and SMGs

Parameter	Unit	ULIRG	SMG
$\log_{10} L_{\text{IR}}$	L_{\odot}	12.0	12.5
R_{eff}	kpc	0.25	1.0
B	mG	1.0	1.0
n_{ISM}	cm^{-3}	2×10^3	1×10^3

these probe more energetic particles (as per Equation (3)). Ionization losses, on the other hand, are enhanced for less energetic particles, and will hence be weaker when probing higher rest-frame frequencies. Since we observe the AS2UDS SMGs at a fixed frequency of $\nu_{\text{obs}} = 1.4$ GHz, the rest-frame frequency probed will be $\nu_{\text{rest}} = 1.4 \times (1 + z)$ GHz. As was noted in Lacki & Thompson (2010), this implies that the observed radio luminosity $L_{\nu_{\text{rest}}}$ will be proportional to $f_{\text{syn}}(\nu_{\text{rest}})$. An observer will then K -correct $L_{\nu_{\text{rest}}}$ to rest-frame 1.4 GHz with a given spectral index. However, since our SMG sample spans a range of redshifts, yet is observed at a fixed frequency, a range of $f_{\text{syn}}(\nu_{\text{rest}})$ is probed, and as such f_{syn} will be a function of redshift. Crucially, this implies that q_{IR} too will vary with redshift as

$$q_{\text{IR}} = q_0 - \log_{10}(f_{\text{syn}}(z)), \quad (7)$$

for some a priori unknown normalization q_0 , under the assumption that the SMG population itself does not evolve significantly with redshift. If the same physical processes are at play in shaping the FIRRC for SMGs and ULIRGs, we can use the observed normalization of the local FIRRC for the latter to model the expected evolution in the correlation for SMGs. In particular, we may write

$$q_{\text{IR}}(z) = 2.64 + \log_{10}\left(\frac{f_{\text{syn}}^{\text{ULIRG}}}{f_{\text{syn}}^{\text{SMG}}(z)}\right), \quad (8)$$

where the normalization of $q_0 = 2.64$ from Bell (2003) was adopted for ULIRGs. We note this is consistent with $q_{\text{IR}} = 2.70 \pm 0.06$ from Farrah et al. (2003) and $q_{\text{IR}} = 2.64 \pm 0.01$ measured by Yun et al. (2001).²²

The parameter f_{syn} is fully determined, under our simplifying assumptions, by the magnetic field strength, ISM density, physical size, FIR luminosity, and redshift of any given source. As such, we adopt a set of standard values for these parameters for both ULIRGs and SMGs, as given in Table 1. We note that the magnetic field strength and particle densities are not particularly well-constrained in either, and as such this “benchmark” model comes with inherent uncertainties. Nevertheless, for simplicity we adopt equal magnetic field strengths of $B = 1.0$ mG for SMGs and ULIRGs, which is consistent with the lower limit of $B \gtrsim 0.2$ mG we determined for SMGs in order to maintain a linear FIRRC in the previous section. We further adopt FIR luminosities typical for the Farrah et al. (2003) and AS2UDS samples for ULIRGs and SMGs, respectively. In addition, we adopt a typical effective radius for the dust emission in SMGs of 1.0 kpc (e.g., Gullberg et al. 2019), and adopt 250 pc for ULIRGs (e.g., Solomon et al. 1997;

²² For Yun et al. (2001), we convert FIR luminosities from 42.5–122.5 μm to the 8–1000 μm range used in this work by adding 0.30 dex, following Bell (2003) and Delhaize et al. (2017).

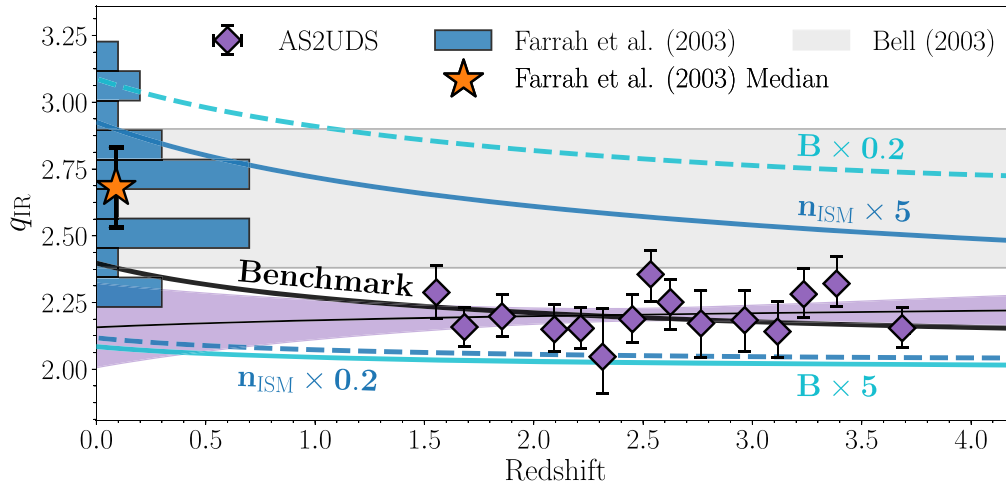


Figure 7. Comparison of the FIRRC for the AS2UDS SMGs with a heterogeneous mix of local, star-forming galaxies (Bell 2003) and local ultra-luminous infrared galaxies (ULIRGs) (Farrah et al. 2003). The AS2UDS points and fit from Figure 5(c) are shown in purple. In addition, five evolutionary toy models for the FIRRC are overlaid. The benchmark model adopts the same magnetic field strength in SMGs and ULIRGs, but assumes the latter are both more compact, and more dense. Four variations are also shown, adopting different magnetic field strengths and densities for SMGs relative to the benchmark model. The increased compactness of ULIRGs compared to $z \sim 2.5$ dusty star-forming galaxies results in higher ionization and inverse Compton losses, and hence in a subdominant contribution from synchrotron emission. This, in turn, gives rise to an increased q_{IR} .

Downes & Solomon 1998). The FIRRC of SMGs, however, is not particularly sensitive to the adopted physical size, since it only affects inverse Compton losses, as per Equation (5). Cosmic rays in the more compact ULIRGs, however, lose a substantially larger fraction of their energy via inverse Compton cooling, as ULIRGs have FIR luminosities comparable to those of SMGs, yet condensed into a smaller volume. Given their increased compactness, we additionally adopt a larger typical ISM density in ULIRGs than in SMGs, although we stress both are inherently uncertain. Given these limitations, we do not aim to make strong predictions on the physical conditions in either ULIRGs or SMGs, but instead use this simplified model to explain global trends in their FIRRC.

We plot the expected $q_{\text{IR}}(z)$ for SMGs, normalized to the local FIRRC for ULIRGs, in Figure 7. In addition, we indicate how this trend is affected by an increase/decrease in B or n_{ISM} by a factor of five. It is clear that our benchmark model recovers the correct normalization of the FIRRC for SMGs. In addition, the frequency dependence of the cooling times induces a slight redshift dependence which, if fitted by $q_{\text{IR}} \propto (1+z)^\gamma$, implies that $\gamma \approx -0.05$, which is marginally consistent with our results. Note that an extrapolation of this model to $z=0$ results in a typical $q_{\text{IR}} \approx 2.4$, which is below the local FIRRC. This should, however, not be interpreted as the predicted normalization for local ULIRGs. Instead, this is the typical q_{IR} an SMG would have when a rest-frame frequency of 1.4 GHz is probed directly.

The variations on the benchmark model in Figure 7 indicate that q_{IR} is substantially affected by changes in the density or magnetic field strength. Increasing the latter naturally increases the relative contribution of synchrotron emission to the overall cosmic ray energy loss, and as such decreases q_{IR} (Equation (7)). Decreasing the density has an analogous effect, as the relative contribution of ionization losses is diminished, and hence f_{syn} is enhanced. We emphasize that our benchmark model is simply one of a family of models with the correct behavior, reproducing the normalization and lack of strong redshift evolution in the FIRRC for SMGs. However, all such models require that synchrotron emission be dominant in

SMGs, with a subdominant contribution from ionization losses. A large value of $f_{\text{syn}} \gtrsim 0.6$ is additionally required to obtain a relatively flat slope in the q_{IR} -redshift plane. In ULIRGs, however, synchrotron emission is subdominant ($f_{\text{syn}} < 0.5$), and instead substantial contributions from ionization and inverse Compton losses ensure that their FIRRC is offset from that of SMGs, and is consistent with that of typical star-forming galaxies observed locally.

The interpretation that synchrotron emission is subdominant in ULIRGs implies that these should have flatter radio spectral indices compared to SMGs due to the increased importance of ionization losses, at comparable rest-frame frequencies. This is in agreement with results in the literature, which indicate that ULIRGs typically show a 1.4–5 GHz spectral index of $\alpha \approx -0.50$ to -0.60 (Clemens et al. 2008; Leroy et al. 2011; Galvin et al. 2016; Klein et al. 2018). Our 610 MHz – 1.4 GHz observations of $z \sim 2$ –3 SMGs probe identical rest-frame frequencies as the higher-frequency data for local ULIRGs, but these instead show a steeper $\alpha \approx -0.80$. While Clemens et al. (2008) interpret this flattening in ULIRGs as the result of increased free-free absorption, they note that ionization losses will have a similar effect on the spectral index. Since no such flattening is observed in SMGs at identical rest-frame frequencies, we prefer the latter interpretation. While we rely mostly on stacked spectral indices in this work, the combination of matched-depth 610 MHz and 1.4 GHz observations of SMGs will provide a suitable means to investigate this in additional detail.

The fact that synchrotron emission is subdominant in ULIRGs further implies that the intrinsic scatter about their FIRRC is likely to be enhanced, as small deviations in, e.g., the magnetic field strength or density will have a relatively large impact on the observed f_{syn} , and in turn on the q_{IR} of individual sources. Such an increase in the scatter about the FIRRC at high FIR luminosities has been widely observed (Helou et al. 1985; Condon et al. 1991a; Yun et al. 2001; Bressan et al. 2002; Bell 2003), and may hence be related to the subdominance of synchrotron emission in ULIRGs. However, Bressan et al. (2002) instead interpret this increased scatter as

being due to a timescale effect, as FIR emission arises on a shorter timescale than radio emission after the onset of star formation. If ULIRGs constitute strong yet relatively short-lived starbursts, the scatter about their FIRRC will be enhanced compared to that of more continuously star-forming systems. In order to test these interpretations, an indicator of the starburst age is required. Multifrequency radio observations may provide a way forward here too, as spectral indices form a proxy for starburst age. In combination with other age indicators, such as star formation rate tracers that probe different timescales, it is possible to begin reconstructing the recent star formation history observationally. In addition, with multifrequency radio observations one can eliminate the inherent uncertainties arising from the intrinsic scatter expected about the FIRRC when a fixed spectral index is assumed.

5. Conclusions

We have presented a study of the FIRRC for AS2UDS (Stach et al. 2019; Dudzevičiūtė et al. 2020): a homogeneously selected sample of 706 SMGs identified through ALMA band 7 follow-up of SCUBA-2 850 μm observations of the UKIDSS/UDS field. Through combining these submillimeter data with deep ($\sigma_{\text{rms}} \sim 7 \mu\text{Jy beam}^{-1}$) VLA radio observations at 1.4 GHz and available 610 MHz coverage from the GMRT, we study their joint FIR and radio properties within the redshift range $1.5 \leq z \leq 4.0$, where our selection is uniform in terms of dust mass or FIR luminosity.

We address the incompleteness in the radio observations through a stacking analysis, and find a typical FIRRC parameter $q_{\text{IR}} = 2.20 \pm 0.03$ for SMGs, which is ~ 0.4 dex lower than the local value for a heterogeneous mix of star-forming galaxies (Bell 2003) and ULIRGs (Yun et al. 2001; Farrah et al. 2003). This value of q_{IR} further shows no evidence of evolution between $1.5 \leq z \leq 4.0$, which likely illustrates that SMGs are a physically homogeneous population of galaxies across redshift, for which no strong redshift evolution is expected.

This offset for SMGs with respect to the local FIRRC is unlikely to be the result of residual contamination by radio AGNs, which is more likely to affect radio-selected samples. Instead, we interpret the offset with respect to the FIRRC of normal galaxies through strong magnetic fields in SMGs ($B \gtrsim 0.2 \text{ mG}$), combined with the production of secondary cosmic rays, both of which serve to increase the radio output of a galaxy for a given star formation rate (Lacki et al. 2010; Lacki & Thompson 2010). Combined high-resolution radio and FIR observations of a large sample of SMGs will provide a robust way to test this interpretation in the future. We additionally model the offset in the FIRRC between SMGs and local ULIRGs, under the assumption that the same physical processes are at play in either. In particular, a model wherein ULIRGs are denser and more compact than SMGs can fully explain the observed offset, as well as the lack of evolution in the FIRRC of SMGs. A prediction of this interpretation is that SMGs have steeper GHz radio spectral indices than ULIRGs, and a reduced scatter about their FIRRC. We argue that matched-depth, multifrequency radio observations of SMGs are crucial in order to test both of these predictions.

We wish to thank the anonymous referee for their comments and suggestions which have improved this work. H.S.B.A., J.A.H., and D.v.d.V. acknowledge support of the VIDI research

program with project number 639.042.611, which is (partly) financed by the Netherlands Organization for Scientific Research (NWO). I.S., U.D., A.M.S., and S.S. acknowledge support from STFC (ST/T000244/1). E.d.C. gratefully acknowledges the Australian Research Council as the recipient of a Future Fellowship (project FT150100079). C.C.C. acknowledges support from the Ministry of Science and Technology of Taiwan (MOST 109-2112-M-001-016-MY3). J.L.W. acknowledges support from an STFC Ernest Rutherford Fellowship (ST/P004784/1 and ST/P004784/2). The National Radio Astronomy Observatory is a facility of the National Science Foundation operated under cooperative agreement by Associated Universities, Inc. The ALMA data used in this paper were obtained under programs ADS/JAO.ALMA#2012.1.00090.S, #2015.1.01528.S and #2016.1.00434.S. ALMA is a partnership of ESO (representing its member states), NSF (USA) and NINS (Japan), together with NRC (Canada) and NSC and ASIAA (Taiwan), in cooperation with the Republic of Chile. The Joint ALMA Observatory is operated by ESO, AUI/NRAO, and NAOJ.

Appendix A Stacking

Throughout this work, we employ a stacking technique in order to incorporate the radio-undetected population. While in principle a straightforward procedure, in practice stacking involves a variety of choices. In particular, the first choice one must make is whether to adopt either the mean or median when stacking. In this work, we adopt the latter, as the median is considerably less affected by outliers in the underlying distribution of flux densities (e.g., White et al. 2007). In addition, Condon et al. (2013) show that the mean is likely to be significantly affected by sources close to the survey detection limit, and as such may be less representative of the full underlying population. We have verified, however, that our results are unchanged when adopting a clipped-mean stacking procedure, whereby SMGs with nearby bright radio sources are omitted from the stacking. While this agreement is encouraging, we still prefer the median as it does not require a (somewhat arbitrary) rejection of sources when stacking, in addition to the reasons elaborated above.

A second choice one must make is how to measure stacked flux densities. In radio astronomy, typically the peak flux density is adopted for a source that is unresolved, while the integrated flux density is utilized for extended sources. Ideally, for a set of unresolved radio sources, one would simply take the pixel value at the location of the SMG, which is equivalent to adopting the peak flux density when all sources are perfectly aligned, in the absence of noise. We show the distribution of peak pixel values in the 1.4 GHz map for the AS2UDS SMGs in Figure A1, and further verify that the fluxes in the off-source stacks used for determining the background and rms noise level are Gaussian and centered around zero. The distribution of fluxes at the AS2UDS source positions are consistent with a power law at high flux densities, and are dominated by the local Gaussian noise in the mosaic at flux densities near the typical rms in the map.

However, these peak-pixel flux densities are likely to underestimate the true flux density of our stacks, as there might be spatial offsets between the radio and FIR emission—either real or as a result of the local noise in the maps. In addition, the sources are not expected to be perfectly unresolved—for instance, at a resolution of $1''.8 \times 1''.6$ at

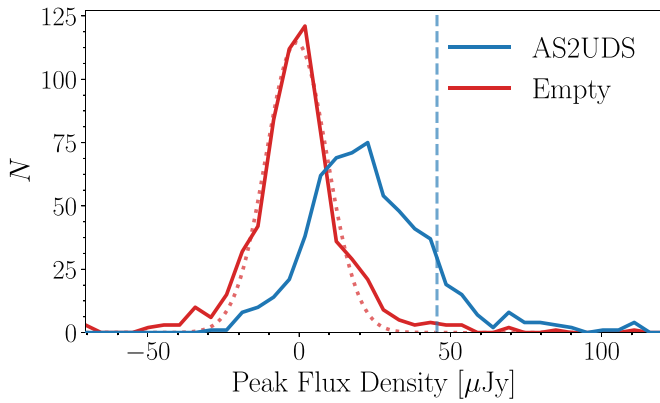


Figure A1. Distribution of peak-pixel flux densities for the AS2UDS SMGs, and empty background regions. The red dotted line shows a Gaussian fit to the latter, with a mean of approximately zero, and the vertical dashed line indicates the detection limit (4σ) at 1.4 GHz. The peak-pixel values for AS2UDS show a clear positive excess, indicative of a large number of sources below the detection limit.

1.4 GHz, nearly half of the radio-detected AS2UDS SMGs are (marginally) resolved at the 3σ level, based on their deconvolved source sizes (following Thomson et al. 2019). As such, integrated flux densities are likely to be more appropriate for the AS2UDS stacks at 1.4 GHz. This is further substantiated by the fact that the integrated flux densities for the stacks of the full AS2UDS sample in Figure 5 exceed the peak flux density by a typical factor of $S_{\text{int}}/S_{\text{peak}} = 1.64 \pm 0.08$. However, in order to determine integrated flux densities, one typically fits Gaussians to the stacked detections, which in turn may be biased when the stacks are at low S/N. We investigate this via a mock-stacking procedure, whereby we insert faint (i.e., including flux densities well below the detection limit) mock sources into the UDS 1.4 GHz map, stack them, and compare both the inserted and recovered flux densities, as well as the recovered peak and integrated values. We adopt a power-law distribution in inserted mock source flux densities with a slope of -2 , which is typical for radio number counts for star-forming sources in the sub-milliJansky regime (e.g., Prandoni et al. 2018), and is additionally consistent with the distribution of peak pixel fluxes shown in Figure A1. The number of sources sampled from this distribution is further varied between $N = 30$ – 100 in order to match the typical number of sources stacked in this work. We then compare the results of two runs: in the first, mock sources are inserted as unresolved, while in the second 40% of mock sources are slightly resolved, randomly being assigned a Gaussian size between 1.2 – $1.6\times$ the beam size. In addition, in order to mimic a true survey, the cataloged mock source positions—those which are used for stacking—are slightly different from the true mock source positions, as we randomly draw an offset in both R.A.

and decl. from a Gaussian distribution with zero mean and standard deviation of $\sigma = 0''.30$. This positional offset is consistent with the observed distribution of separations between the FIR and radio positions of the AS2UDS sources with radio counterparts at 1.4 GHz.

We compare the two mock-stacking runs in Figure A2, where we quantify the difference between recovered integrated and peak flux densities, as well as the level of “flux boosting,” that is, the ratio of the recovered and inserted flux density. For unresolved mock sources, the integrated-to-peak ratio is typically slightly larger than unity, indicating that at a modest $S/N \lesssim 10$, integrated flux densities may be slightly overestimated. However, at the typical $S/N \sim 8.5$ – 15 we obtain for the AS2UDS stacks, $S_{\text{int}}/S_{\text{peak}} = 1.18 \pm 0.02$ for the unresolved mock sources, while the real data indicate a much higher value of $S_{\text{int}}/S_{\text{peak}} = 1.64 \pm 0.08$. This implies that the peak flux density does not constitute an accurate measurement of the true stacked flux density. Instead, if we allow for resolved sources and random positional offsets, we find that the typical $S_{\text{int}}/S_{\text{peak}}$ we obtain for the AS2UDS sample is accurately recovered by the simulated stacks. In this case, peak flux densities underestimate the true radio flux density by a factor of 0.74 ± 0.11 , which in turn leads to q_{IR} being overestimated by a typical $\Delta q_{\text{IR}} = 0.13 \pm 0.06$, where the uncertainty represents the standard deviation across the stacked mock sources. However, in the S/N range achieved for AS2UDS, we find $\Delta q_{\text{IR}} = -0.05 \pm 0.08$ for the integrated flux density. As such, total fluxes from Gaussian fits constitute a better measurement of the true radio flux of the AS2UDS SMGs than peak flux densities. Conversely, the measured AS2UDS stacks in the GMRT 610 MHz map shown in Figure 4 have an average ratio of their integrated-to-peak flux density of $S_{\text{int}}/S_{\text{peak}} = 1.07 \pm 0.05$. This value is consistent with a value of unity, and hence with the stacks being unresolved—as may be expected given the large beam size of the GMRT observations. We therefore adopt the peak flux density for the GMRT stacks in this work. We have additionally verified through stacking of simulated sources that these peak flux densities are reliable for the GMRT data.

Figure A2 further indicates that at low S/N, the integrated flux density becomes increasingly biased, and tends to overestimate the true flux density, similar to what was observed by Leslie et al. (2020). While we investigate this in more detail in a forthcoming paper, in this work we ensure the stacks are all of high S/N ($\gtrsim 10$) in order for reliable integrated flux density measurements to be made. As a representative example, we show in Figure A3 the stacks and residuals corresponding to the stacked data for the full AS2UDS sample in Figure 5. The featureless residuals show the integrated flux density measurements to be accurate.

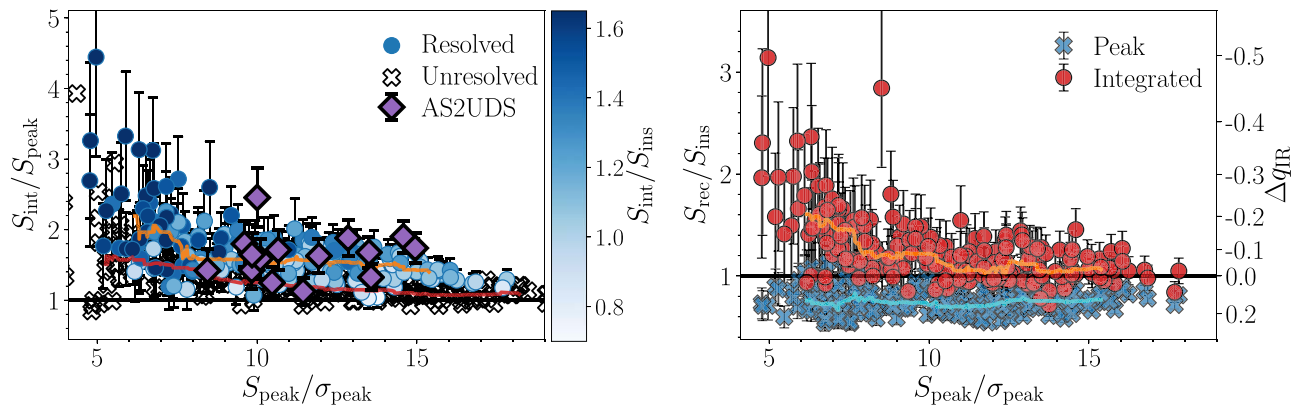


Figure A2. Left: ratio of the recovered integrated and peak flux densities of the stacked mock sources, as a function of peak S/N. The data are colored by the magnitude of flux boosting. Black crosses correspond to stacking of unresolved mock sources only, while the circles include resolved sources, as well as small, random positional offsets between the true and cataloged source centers. The running median through the circles (crosses) is shown via the orange (red) line. The stacked AS2UDS SMGs (purple diamonds) show a substantially larger typical integrated-to-peak flux density ratio than the unresolved mock sources. Right: ratio of recovered/integrated flux density vs. recovered peak S/N. The orange (blue) line indicates the running median through the points representing integrated (peak) flux density measurements, and the right ordinate axis shows the propagated offset in q_{IR} based on the difference in the true and recovered flux densities. Overall, the integrated value constitutes a better estimate of the true flux density of the stacks at $S/N \gtrsim 10$.

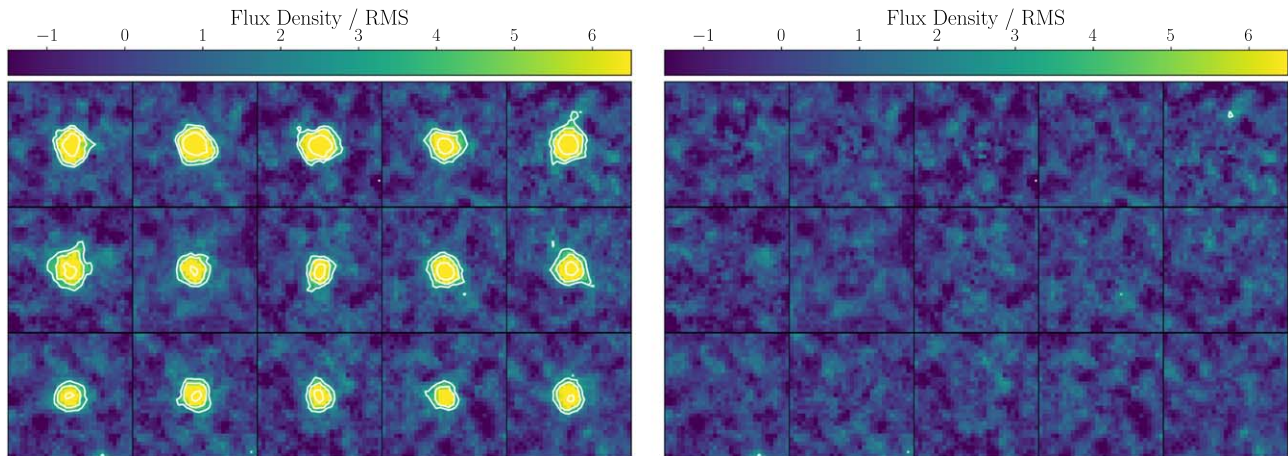


Figure A3. Left: stacked detections for the 15 bins shown in Figure 5(c), combining 222 and 418 radio-detected and -undetected sources, respectively. Only the central 31×31 pixels ($11'' \times 11''$) are shown, for clarity. The color scheme runs from -1.5 to 6.5σ , where σ is the rms noise in the stack. Contours are shown at levels of -3 (dashed) and $3, 5, 9\sigma$ (solid). Right: residuals, after fitting the stacked detections with an elliptical Gaussian via PYBDSF (Mohan & Rafferty 2015). All stacks show a detection at a high median S/N of 11σ , and are well-fit by the Gaussian model as demonstrated by the featureless residuals.

Appendix B

Radio AGNs in Submillimeter- and Radio-selected Samples

By construction, radio-selected studies are sensitive to the combined emission from star formation and AGN activity, whereas submillimeter surveys are restricted solely to dust-obscured star formation. As such, a higher incidence of radio-excess AGNs may naturally be expected in radio-selected samples.

We show in the left panel of Figure B1 the fraction of radio-excess AGNs in both AS2UDS and two 3 GHz-selected radio samples (Smolčić et al. 2017b; Algera et al. 2020) as a function of radio flux density. In the latter two studies, AGNs were similarly identified via a radio-excess criterion, though by adopting a redshift-dependent radio-excess threshold instead of the fixed value we adopt in this work. For the radio studies, we scale flux densities from 3 to 1.4 GHz assuming a spectral index of $\alpha = -0.70$ (following, e.g., Smolčić et al. 2017a).

At the faint end of AS2UDS, $S_{1.4} \sim 50 \mu\text{Jy}$, Algera et al. (2020) find that radio-excess AGNs still make up $\sim 10\%$ of the radio population, while the AGN fraction in the SMGs in this

regime is consistent with zero. At higher flux densities $S_{1.4} \sim 300 \mu\text{Jy}$, Smolčić et al. (2017b) determine AGN fractions of $\sim 50\%$, compared to the $\sim 10\%$ for the radio-detected AS2UDS sample. This emphasizes that, while both radio and FIR emission are tracers of star formation, the former suffers significant contamination. The increased incidence of radio-excess AGNs in radio surveys is not surprising—after all, these constitute some of the brightest radio sources observed. However, it suggests that studies of the FIRRC based on radio-selected samples will be biased by contamination from AGNs. In particular, such surveys will be more sensitive to composite sources, where radio emission from both AGN activity and star formation contributes to the overall radio luminosity, compared to a submillimeter-selected sample. This is further demonstrated in the right panel of Figure B1, where we show the radio-AGN fraction as a function of $870 \mu\text{m}$ flux density. We find no evidence for any correlation, and a linear fit through the data returns a slope of $(2.2 \pm 2.3) \times 10^{-3}$, consistent with no gradient at the 1σ level. This substantiates that a FIR-based selection renders the sample insensitive to radio AGNs.

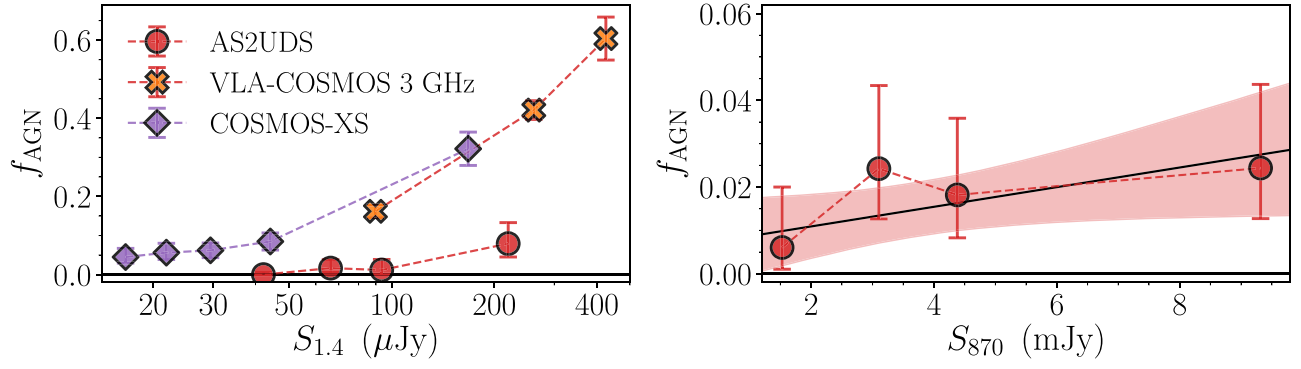


Figure B1. Left: distribution of radio-excess AGNs as a function of 1.4 GHz flux density. The full radio-detected AS2UDS sample is subdivided into four different bins, from which AGNs are identified as having $q_{\text{IR}} \leq 1.55$. The uncertainty on the points represents the counting error from Gehrels (1986). At flux densities $S_{1.4} \lesssim 100 \mu\text{Jy}$, the AGN fraction is only $f_{\text{AGN}} = 1_{-1}^{+2}\%$. For comparison, we overplot fractions of radio-excess AGNs from two deep radio surveys at 3 GHz (scaled to 1.4 GHz using $\alpha = -0.70$): COSMOS-XS (Algera et al. 2020; Van der Vlugt et al. 2020) in purple and VLA-COSMOS (Smolčić et al. 2017a, 2017b) in orange. The incidence of radio-excess AGNs in such radio-selected samples is an order of magnitude larger than in the AS2UDS SMG sample. Right: distribution of radio-excess AGNs as a function of 870 μm flux density, for the full AS2UDS sample, including the radio-undetected population. The red shaded region represents a linear fit through the data, and shows no evidence of a trend between the incidence of radio AGNs and submillimeter flux.

Appendix C The FIRRC in Radio-selected Samples

As outlined in Section 4.1, radio-selected samples typically observe a declining q_{IR} with redshift, whereas we observe no such evolution in our sample of SMGs. A likely explanation is that this evolution toward lower values of q_{IR} is the result of (low-level) AGN emission (Murphy 2009). However, obtaining conclusive evidence for this is complicated by the fact that, by definition, these AGNs are very difficult to identify in radio surveys. One clear way to distinguish AGNs from purely star-forming sources in the radio, however, is through VLBI observations, which are sensitive only to strong and compact sources of radio emission. If we assume the evolution in the FIRRC seen in recent radio surveys is solely due to low-level radio AGNs, we can calculate the redshift-dependent fraction of radio emission that originates from star formation. This further requires the assumption that FIR emission is a perfect tracer of star formation rate across all redshifts. Given a local “correct” value of q_{IR} equal to q_0 , as well as redshift evolution with slope γ , as defined in Section 3.3, the average redshift-dependent fraction of radio emission that originates from star formation, f_{SFR} , is equal to

$$f_{\text{SFR}}(z) = 10q_0^{(1+z)^\gamma - 1}. \quad (\text{C1})$$

Herrera Ruiz et al. (2017) observed the 2 deg² COSMOS field with VLBI observations at 1.4 GHz, reaching a sensitivity of $\sigma \sim 10\text{--}15 \mu\text{Jy}$, similar to that of the original 1.4 GHz VLA COSMOS survey (Schinnerer et al. 2007, 2010). They identify 438 radio sources at $\geq 5.5\sigma$ significance, with a typical VLBI flux density of $\sim 0.6\text{--}0.7$ times the total flux density, obtained from the lower-resolution VLA observations. This constitutes a typical detection fraction of $f_{\text{det}} \simeq 0.20$ in the VLBI data. Additionally, they find that the sub-millijansky radio population is more likely to host a dominant radio AGN, i.e., contributing a larger fraction of the total radio luminosity, though this is likely to (at least partially) be a selection effect, as faint sources require a strong AGN contribution to be detectable in the VLBI observations in the first place. In the following, we define $f_{\text{AGN}} = 1 - f_{\text{SFR}} = S_{\text{VLBI}}/S_{\text{VLA}}$, following Herrera Ruiz et al. (2017), and we adopt a value of $f_{\text{AGN}} = 0.70$, which is typical for their sample at $S_{\text{VLA}} \lesssim 1\text{mJy}$. Due to the aforementioned selection effects, this likely

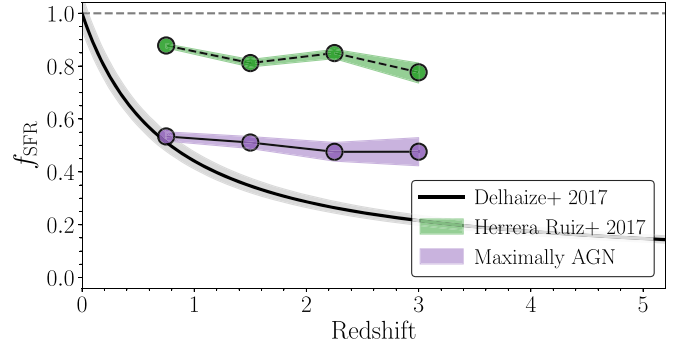


Figure C1. Fractional contribution of star formation to the total radio emission as a function of redshift, under the assumption that the FIRRC is nonevolving, and any observed variation in the correlation is the result of emission from unidentified AGNs. The black line shows the evolution measured by Delhaize et al. (2017), using data from the 3 GHz VLA-COSMOS project. The green shaded region shows the expected fraction of star formation-powered radio emission based on the VLBI observations from Herrera Ruiz et al. (2017), given their detection rate as a function of redshift, and a fixed fraction of $f_{\text{AGN}} = S_{\text{VLBI}}/S_{\text{VLA}} = 0.70$. This region still constitutes a lower limit on f_{SFR} as radio-excess AGNs were not removed from the VLBI sample. The purple shaded region constitutes the expected f_{SFR} when all VLBI-undetected sources in the 1.4 GHz VLA COSMOS project (Schinnerer et al. 2007, 2010) have the maximum possible AGN contribution to render them just below the VLBI detection limit. Even this unrealistic scenario cannot explain the measured redshift dependence of the FIRRC in radio studies beyond $z \gtrsim 1.5$, and hence an enhanced AGN contribution at high redshift alone is unlikely to be enough to fully account for the observed evolution in the FIRRC seen in radio-based samples.







constitutes an upper limit to the actual contribution from a typical AGN within this flux density range. Additionally, we do not explicitly remove radio-excess AGNs from this sample, which are typically discarded prior to calculating the FIRRC, and as a result, the calculated f_{AGN} in this way will constitute a rather strict upper limit.

We show in Figure C1 the expected f_{SFR} as a function of redshift, assuming the evolution in the FIRRC found by Delhaize et al. (2017) is solely the result of unidentified AGN contamination. We overplot the expected contribution from AGNs based on the Herrera Ruiz et al. (2017) VLBI sample, as well as the f_{SFR} expected when *all* sources from the 1.4 GHz VLA COSMOS survey that are undetected in the VLBI

observations have the maximal possible AGN contribution to render them just below the detection limit, i.e., $f_{\text{AGN}}^{\text{max}} = 5.5 \times \sigma_{\text{RMS}}/S_{\text{VLA}}$. This, evidently, constitutes a highly unrealistic scenario. The VLBI sample from Herrera Ruiz et al. (2017) implies an upper limit on the fraction of AGN contamination on the order of 20%. Additionally, this fraction is not a strong function of redshift, as the fraction of known radio sources they detect in the VLBI observations does not vary much across cosmic time. While the “maximally AGN” scenario coincides with the expected f_{SFR} at $z \sim 1$, the lack of a redshift dependence ensures that at higher redshifts even this worst-case scenario underestimates how much AGNs are required to contribute in order to obtain the observed redshift evolution in the FIRRC in radio-selected samples.

Overall, an enhanced AGN contribution at high redshift alone is therefore unlikely to fully account for the observed evolution in the FIRRC seen in radio surveys, and even by requiring all VLBI-undetected sources to be radio AGNs, we cannot explain the observed f_{SFR} . As a result, it is likely that the difference between the FIRRCs for radio-selected and submillimeter-selected samples is due to the different galaxy populations such studies probe.

ORCID iDs

H. S. B. Algera  <https://orcid.org/0000-0002-4205-9567>
 I. Smail  <https://orcid.org/0000-0003-3037-257X>
 A. M. Swinbank  <https://orcid.org/0000-0003-1192-5837>
 S. Stach  <https://orcid.org/0000-0003-1122-6948>
 J. A. Hodge  <https://orcid.org/0000-0001-6586-8845>
 O. Almaini  <https://orcid.org/0000-0001-9328-3991>
 A. W. Blain  <https://orcid.org/0000-0001-7489-5167>
 D. Scott  <https://orcid.org/0000-0002-6878-9840>
 J. L. Wardlow  <https://orcid.org/0000-0003-2376-8971>

References

- Algera, H. S. B., Van der Vlugt, D., & Hodge, J. A. 2020, *ApJ*, 903, 139
 Barger, A. J., Cowie, L. L., Sanders, D. B., et al. 1998, *Natur*, 394, 248
 Barger, A. J., Wang, W. H., Cowie, L. L., et al. 2012, *ApJ*, 761, 89
 Battisti, A. J., da Cunha, E., Grasha, K., et al. 2019, *ApJ*, 882, 61
 Beck, R., & Wielebinski, R. 2013, *Magnetic Fields in Galaxies* (Dordrecht: Springer), 641
 Bell, E. F. 2003, *ApJ*, 586, 794
 Beswick, R. J., Muxlow, T. W. B., Thrall, H., Richards, A. M. S., & Garrington, S. T. 2008, *MNRAS*, 385, 1143
 Biggs, A. D., Ivison, R. J., Ibar, E., et al. 2011, *MNRAS*, 413, 2314
 Biggs, A. D., Younger, J. D., & Ivison, R. J. 2010, *MNRAS*, 408, 342
 Blain, A. W., Smail, I., Ivison, R. J., Kneib, J. P., & Frayer, D. T. 2002, *PhR*, 369, 111
 Bonzini, M., Padovani, P., Mainieri, V., et al. 2013, *MNRAS*, 436, 3759
 Bothwell, M. S., Smail, I., Chapman, S. C., et al. 2013, *MNRAS*, 429, 3047
 Bressan, A., Silva, L., & Granato, G. L. 2002, *A&A*, 392, 377
 Calistro Rivera, G., Williams, W. L., Hardcastle, M. J., et al. 2017, *MNRAS*, 469, 3468
 Carilli, C. L., & Barthel, P. D. 1996, *A&ARv*, 7, 1
 Carilli, C. L., & Yun, M. S. 1999, *ApJL*, 513, L13
 Chabrier, G. 2003, *PASP*, 115, 763
 Chapman, S. C., Blain, A. W., Smail, I., & Ivison, R. J. 2005, *ApJ*, 622, 772
 Chen, H., Garrett, M. A., Chi, S., et al. 2020, *A&A*, 638, A113
 Clemens, M. S., Vega, O., Bressan, A., et al. 2008, *A&A*, 477, 95
 Condon, J. J. 1989, *ApJ*, 338, 13
 Condon, J. J. 1992, *ARA&A*, 30, 575
 Condon, J. J., Anderson, M. L., & Helou, G. 1991a, *ApJ*, 376, 95
 Condon, J. J., & Broderick, J. J. 1986, *AJ*, 92, 94
 Condon, J. J., & Broderick, J. J. 1991, *AJ*, 102, 1663
 Condon, J. J., Huang, Z. P., Yin, Q. F., & Thuan, T. X. 1991b, *ApJ*, 378, 65
 Condon, J. J., Kellermann, K. I., Kimball, A. E., Ivezić, Ž., & Perley, R. A. 2013, *ApJ*, 768, 37
 Crain, R. A., Schaye, J., Bower, R. G., et al. 2015, *MNRAS*, 450, 1937
 da Cunha, E., Charlot, S., & Elbaz, D. 2008, *MNRAS*, 388, 1595
 da Cunha, E., Walter, F., Smail, I. R., et al. 2015, *ApJ*, 806, 110
 Danielson, A. L. R., Swinbank, A. M., Smail, I., et al. 2017, *ApJ*, 840, 78
 Decarli, R., Smail, I., Walter, F., et al. 2014, *ApJ*, 780, 115
 de Jong, T., Klein, U., Wielebinski, R., & Wunderlich, E. 1985, *A&A*, 147, L6
 Delhaize, J., Smolčić, V., Delvecchio, I., et al. 2017, *A&A*, 602, A4
 Del Moro, A., Alexander, D. M., Mullaney, J. R., et al. 2013, *A&A*, 549, A59
 Delvecchio, I., Smolčić, V., Zamorani, G., et al. 2017, *A&A*, 602, A3
 Downes, D., & Solomon, P. M. 1998, *ApJ*, 507, 615
 Dudzevičiūtė, U., Smail, I., Swinbank, A. M., et al. 2020, *MNRAS*, 494, 3828
 Duncan, K. J., Shivaee, I., Shapley, A. E., et al. 2020, *MNRAS*, 498, 3648
 Farrah, D., Afonso, J., Efstathiou, A., et al. 2003, *MNRAS*, 343, 585
 Galvin, T. J., Seymour, N., Filipović, M. D., et al. 2016, *MNRAS*, 461, 825
 Galvin, T. J., Seymour, N., Marvil, J., et al. 2018, *MNRAS*, 474, 779
 Geach, J. E., Dunlop, J. S., Halpern, M., et al. 2017, *MNRAS*, 465, 1789
 Gehrels, N. 1986, *ApJ*, 303, 336
 Gim, H. B., Yun, M. S., Owen, F. N., et al. 2019, *ApJ*, 875, 80
 Gullberg, B., Smail, I., Swinbank, A. M., et al. 2019, *MNRAS*, 490, 4956
 Haarsma, D. B., Partridge, R. B., Windhorst, R. A., & Richards, E. A. 2000, *ApJ*, 544, 641
 Hainline, L. J., Blain, A. W., Smail, I., et al. 2011, *ApJ*, 740, 96
 Heger, A., Fryer, C. L., Woosley, S. E., Langer, N., & Hartmann, D. H. 2003, *ApJ*, 591, 288
 Helou, G., Soifer, B. T., & Rowan-Robinson, M. 1985, *ApJL*, 298, L7
 Herrera Ruiz, N., Middelberg, E., Deller, A., et al. 2017, *A&A*, 607, A132
 Hodge, J. A., Karim, A., Smail, I., et al. 2013, *ApJ*, 768, 91
 Hodge, J. A., Swinbank, A. M., Simpson, J. M., et al. 2016, *ApJ*, 833, 103
 Hughes, D. H., Serjeant, S., Dunlop, J., et al. 1998, *Natur*, 394, 241
 Ibar, E., Ivison, R. J., Best, P. N., et al. 2010, *MNRAS*, 401, L53
 Ibar, E., Ivison, R. J., Biggs, A. D., et al. 2009, *MNRAS*, 397, 281
 Ivison, R. J., Alexander, D. M., Biggs, A. D., et al. 2010a, *MNRAS*, 402, 245
 Ivison, R. J., Magnelli, B., Ibar, E., et al. 2010b, *A&A*, 518, L31
 Ivison, R. J., Smail, I., Le Borgne, J. F., et al. 1998, *MNRAS*, 298, 583
 Jarvis, M. J., Smith, D. J. B., Bonfield, D. G., et al. 2010, *MNRAS*, 409, 92
 Jiménez-Andrade, E. F., Magnelli, B., Karim, A., et al. 2019, *A&A*, 625, A114
 Karim, A., Schinnerer, E., Martínez-Sansigre, A., et al. 2011, *ApJ*, 730, 61
 Karim, A., Swinbank, A. M., Hodge, J. A., et al. 2013, *MNRAS*, 432, 2
 Kennicutt, R. C. J. 1998, *ARA&A*, 36, 189
 Klein, U., Lisenfeld, U., & Verley, S. 2018, *A&A*, 611, A55
 Kocevski, D. D., Hasinger, G., Brightman, M., et al. 2018, *ApJS*, 236, 48
 Kovács, A., Chapman, S. C., Dowell, C. D., et al. 2006, *ApJ*, 650, 592
 Lacki, B. C., & Thompson, T. A. 2010, *ApJ*, 717, 196
 Lacki, B. C., Thompson, T. A., & Quataert, E. 2010, *ApJ*, 717, 1
 Lee, S.-K., Ferguson, H. C., Somerville, R. S., Wiklund, T., & Gialalisco, M. 2010, *ApJ*, 725, 1644
 Leroy, A. K., Evans, A. S., Momjian, E., et al. 2011, *ApJL*, 739, L25
 Leslie, S. K., Schinnerer, E., Liu, D., et al. 2020, *ApJ*, 899, 58
 Lindner, R. R., Baker, A. J., Omont, A., et al. 2011, *ApJ*, 737, 83
 Lisenfeld, U., Völk, H. J., & Xu, C. 1996, *A&A*, 306, 677
 Lyu, J., & Rieke, G. H. 2017, *ApJ*, 841, 76
 Magnelli, B., Ivison, R. J., Lutz, D., et al. 2015, *A&A*, 573, A45
 Magnelli, B., Lutz, D., Berta, S., et al. 2010, *A&A*, 518, L28
 Mao, M. Y., Huynh, M. T., Norris, R. P., et al. 2011, *ApJ*, 731, 79
 McAlpine, S., Smail, I., Bower, R. G., et al. 2019, *MNRAS*, 488, 2440
 McBride, J., Quataert, E., Heiles, C., & Bauermeister, A. 2014, *ApJ*, 780, 182
 McBride, J., Robishaw, T., Heiles, C., Bower, G. C., & Sarma, A. P. 2015, *MNRAS*, 447, 1103
 Michałowski, M. J., Dunlop, J. S., Cirasuolo, M., et al. 2012, *A&A*, 541, A85
 Middelberg, E., Deller, A. T., Norris, R. P., et al. 2013, *A&A*, 551, A97
 Miettinen, O., Novak, M., Smolčić, V., et al. 2017, *A&A*, 602, A54
 Mohan, N., & Rafferty, D. 2015, PyBDSF: Python Blob Detection and Source Finder, Astrophysics Source Code Library, ascl:1502.007
 Molnár, D. C., Sargent, M. T., Delhaize, J., et al. 2018, *MNRAS*, 475, 827
 Momjian, E., Wang, W.-H., Knudsen, K. K., et al. 2010, *AJ*, 139, 1622
 Murphy, E. J. 2009, *ApJ*, 706, 482
 Murphy, E. J., Chary, R. R., Alexander, D. M., et al. 2009, *ApJ*, 698, 1380
 Murphy, E. J., Condon, J. J., Schinnerer, E., et al. 2011, *ApJ*, 737, 67
 Muxlow, T. W. B., Richards, A. M. S., Garrington, S. T., et al. 2005, *MNRAS*, 358, 1159
 Muxlow, T. W. B., Thomson, A. P., Radcliffe, J. F., et al. 2020, *MNRAS*, 495, 1188
 Niklas, S., Klein, U., & Wielebinski, R. 1997, *A&A*, 322, 19
 Novak, M., Smolčić, V., Delhaize, J., et al. 2017, *A&A*, 602, A5

- Ocran, E. F., Taylor, A. R., Vaccari, M., et al. 2020, *MNRAS*, **491**, 5911
- Padovani, P., Mainieri, V., Tozzi, P., et al. 2009, *ApJ*, **694**, 235
- Prandoni, I., Guglielmino, G., Morganti, R., et al. 2018, *MNRAS*, **481**, 4548
- Robishaw, T., Quataert, E., & Heiles, C. 2008, *ApJ*, **680**, 981
- Rybak, M., Calistro Rivera, G., Hodge, J. A., et al. 2019, *ApJ*, **876**, 112
- Sargent, M. T., Schinnerer, E., Murphy, E., et al. 2010, *ApJL*, **714**, L190
- Schaye, J., Crain, R. A., Bower, R. G., et al. 2015, *MNRAS*, **446**, 521
- Schinnerer, E., Sargent, M. T., Bondi, M., et al. 2010, *ApJS*, **188**, 384
- Schinnerer, E., Smolčić, V., Carilli, C. L., et al. 2007, *ApJS*, **172**, 46
- Schleicher, D. R. G., & Beck, R. 2013, *A&A*, **556**, A142
- Simpson, J. M., Smail, I., Swinbank, A. M., et al. 2015, *ApJ*, **799**, 81
- Simpson, J. M., Swinbank, A. M., Smail, I., et al. 2014, *ApJ*, **788**, 125
- Smail, I., Dudzevičiūtė, U., & Stach, S. M. 2020, arXiv:2010.02250
- Smail, I., Ivison, R. J., & Blain, A. W. 1997, *ApJL*, **490**, L5
- Smail, I., Ivison, R. J., Owen, F. N., Blain, A. W., & Kneib, J. P. 2000, *ApJ*, **528**, 612
- Smolčić, V. 2009, *ApJL*, **699**, L43
- Smolčić, V., Delvecchio, I., Zamorani, G., et al. 2017b, *A&A*, **602**, A2
- Smolčić, V., Novak, M., Bondi, M., et al. 2017a, *A&A*, **602**, A1
- Smolčić, V., Schinnerer, E., Zamorani, G., et al. 2009, *ApJ*, **690**, 610
- Solomon, P. M., Downes, D., Radford, S. J. E., & Barrett, J. W. 1997, *ApJ*, **478**, 144
- Speagle, J. S., Steinhardt, C. L., Capak, P. L., & Silverman, J. D. 2014, *ApJS*, **214**, 15
- Stach, S. M., Dudzevičiūtė, U., Smail, I., et al. 2019, *MNRAS*, **487**, 4648
- Swinbank, A. M., Simpson, J. M., Smail, I., et al. 2014, *MNRAS*, **438**, 1267
- Tabatabaei, F. S., Schinnerer, E., Krause, M., et al. 2017, *ApJ*, **836**, 185
- Thompson, T. A., Quataert, E., Waxman, E., Murray, N., & Martin, C. L. 2006, *ApJ*, **645**, 186
- Thomson, A. P., Ivison, R. J., Owen, F. N., et al. 2015, *MNRAS*, **448**, 1874
- Thomson, A. P., Ivison, R. J., Simpson, J. M., et al. 2014, *MNRAS*, **442**, 577
- Thomson, A. P., Smail, I., Swinbank, A. M., et al. 2019, *ApJ*, **883**, 204
- Tisanić, K., Smolčić, V., Delhaize, J., et al. 2019, *A&A*, **621**, A139
- van der Kruit, P. C. 1971, *A&A*, **15**, 110
- van der Kruit, P. C. 1973, *A&A*, **29**, 263
- Van der Vlugt, D., Algera, H. S. B., & Hodge, J. A. 2020, arXiv:2009.13528
- Varenus, E., Conway, J. E., Martí-Vidal, I., et al. 2016, *A&A*, **593**, A86
- Völk, H. J. 1989, *A&A*, **218**, 67
- Weiß, A., Kovács, A., Coppin, K., et al. 2009, *ApJ*, **707**, 1201
- White, R. L., Helfand, D. J., Becker, R. H., Glikman, E., & de Vries, W. 2007, *ApJ*, **654**, 99
- Xu, J., Sun, M., & Xue, Y. 2020, *ApJ*, **894**, 21
- Yeast-Hull, T. M., Gallagher, J. S., & Zweibel, E. G. 2016, *MNRAS*, **457**, L29
- Yun, M. S., Hibbard, J. E., Condon, J. J., & Reddy, N. 1999, *Ap&SS*, **266**, 29
- Yun, M. S., Reddy, N. A., & Condon, J. J. 2001, *ApJ*, **554**, 803